https://doi.org/10.1016/j.renene.2021.08.089

Multi-perspective analysis of CO poisoning in high-temperature proton exchange membrane fuel cell stack via numerical investigation

Jun Zhang [1], Caizhi Zhang [1, *], Jin Li [3], Bo Deng [4], Min Fan [5], Meng Ni [2, *], Zhanxin Mao [4], Honggeng Yuan [3]

[1] School of Automotive Engineering; The State Key Laboratory of Mechanical Transmissions; Chongqing Automotive Collaborative Innovation Centre, Chongqing University, Chongqing, China, 400044

[2] Department of Building and Real Estate, Building Energy Research Group, The Hong Kong Polytechnic University, Hung Hom, Kowloon, Hong Kong, China

[3] Chongqing Zongshen Power Machine Co., Ltd., Zongshen Industry Zone, Banan District, Chongqing 400054, China

[4] National Hydrogen Power Quality Supervision and Inspection Center, China Automotive Engineering Research Institute Co., Ltd, Chongqing, China, 401122

[5] Chongqing Changan New Energy Vehicle Technology Co., Ltd, Chongqing, China 400000

(* Corresponding authors at C.Z Zhang, czzhang@cqu.edu.cn; M. Ni, meng.ni@polyu.edu.hk)

Abstract

To comprehensively understand the CO poisoning effect on high-temperature PEMFC stack (HT-PEMFCs), a 3-D numerical HT-PEMFCs model is developed. The crucial anodic kinetic parameters are obtained from experimental data to improve the accuracy of the model. Then, multi-perspective analysis is conducted on different HT-PEMFC stacks with 1, 3, and 5 cells working at 160ºC with 3 mol% CO in H_2. Besides, parametric simulations are conducted on the three-cell stack. It is found that the CO and H_2 coverage varies between cells in the stack due to the temperature distribution difference, and the stack with more cells as well as the middle-cell of multi-cell stack have better performance, higher H_2 coverage, lower CO coverage due to higher internal temperature. However, too high local temperature not only reduce the CO coverage but reduce the H_2 coverage and increase the anode overpotential. The resistance to CO poisoning can be improved by increasing operating temperature, but when CO_2 and water vapor are introduced into the anode, the H_2 coverage decreases and the CO coverage increases due to the decrease of H_2 concentration. The study clearly demonstrated that high performance and high CO resistance can be achieved by carefully regulating the operating conditions.

Keywords: HT-PEMFC stack; CO poisoning; Numerical model; Anodic kinetic parameters; H_2 and CO coverage

Graphical Abstract

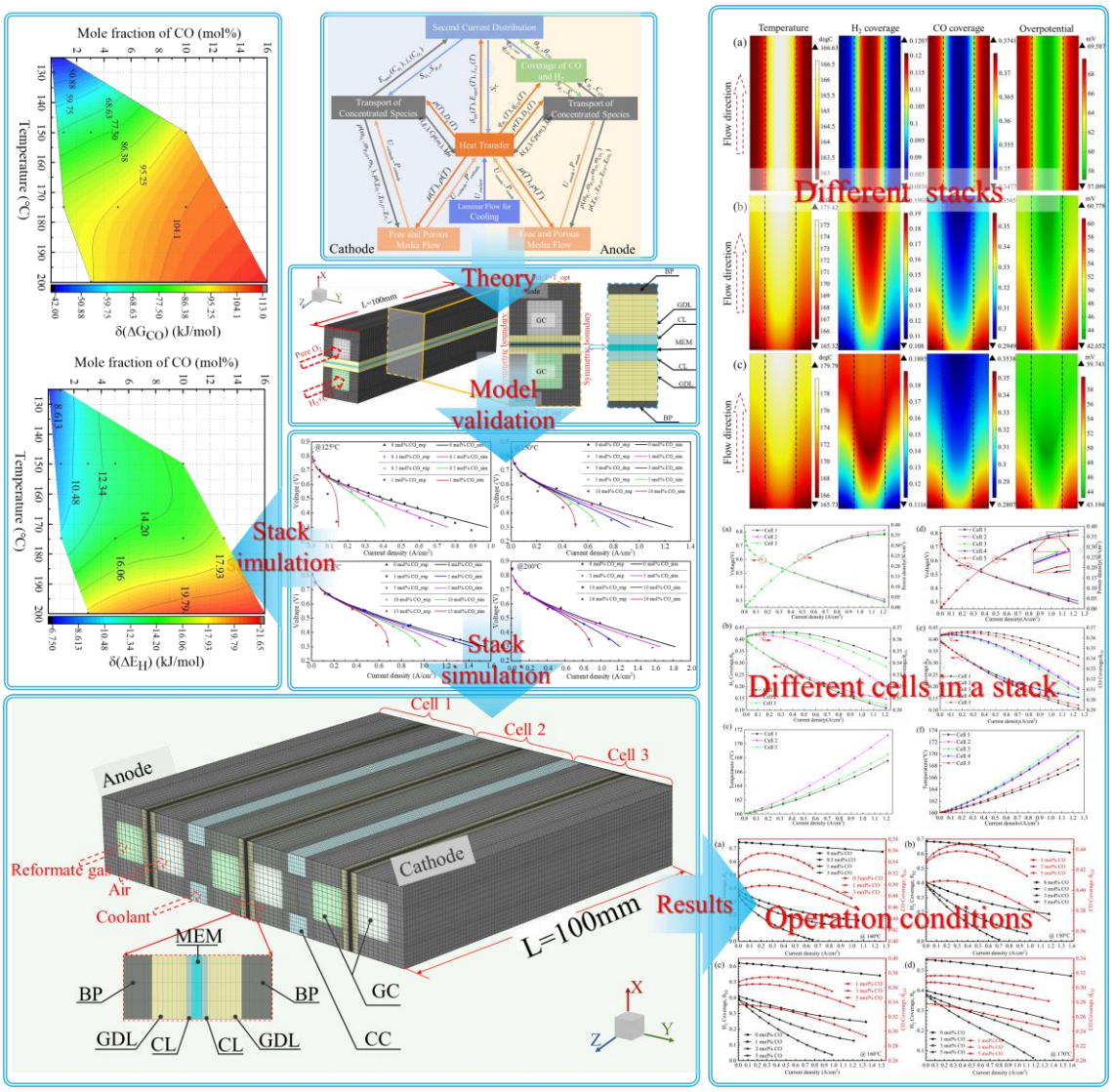

1. Introduction

1.1. Background

Proton exchange membrane fuel cell (PEMFC) is an electrical and thermal power source with high energy conversion efficiency and environmental friendliness, which could help ease or overcome global warming and energy crisis，and plays an important role in the future “Hydrogen Economy” [1-3]. As a secondary energy source, hydrogen (H_2) fails to

be mined directly from nature. Instead, it can be produced by following different processes: 1) electrolyzed water by alkaline water electrolyzer (AWE), proton exchange membrane electrolysis cell (PEMEC) and solid oxide electrolysis cell (SOEC) [4]; 2) steam reforming of natural gas, hydrocarbons, and alcohols [5,6]; 3) gasification of petroleum coke and coal [7]. The first method provides a convenient and quick solution for producing high purity hydrogen, but the cost of water electrolysis is too expensive [8]. While the hydrogen produced by other methods contains many impurities, such as CO, CO_2, H_2O, which requires subsequent gas purification processes. In addition, because of the relatively low energy density of H_2 under normal temperature and pressure and the hydrogen embrittlement problem of metal, the cost and the energy needed to distribute and store H_2 are both expensive [9,10]. High-temperature PEMFC (HT-PEMFC) with polybenzimidazole (PBI)/Phosphoric Acid (PA) membrane can operate in a temperature range of 120~180^{o}C, which has a higher resistance to impurities (especially CO) compared with conventional low-temperature PEMFC (LT-PEMFC) [11], and it can be directly integrated with methanol steam reformer to improve energy efficiency [12]. Besides, the advantages of HT-PEMFC also include simpler water and thermal management, improvement of electrochemical kinetics (especially at the cathode), lower cost due to possible use of non-noble metal catalyst, and easy waste heat recovery via combined heating and power (CHP) systems [13-15]. However, there are still some challenges hindering its widespread commercialization, such as durability issue caused by the degradation of the components under acidic conditions and high temperature [16], long start-up time since the temperature has to be raised above 100^{o}C (the boiling point of water) to avoid loss of phosphoric acid [17]. Therefore, it has attracted great interest in the fuel cell community all over the world, since the concept of HT-PEMFC was proposed in the early 1990s [18,19].

Therefore, considerable research has been done to promote the development and application of HT-PEMFC during the past three decades. Water and heat management [20], start-up processes from room temperature [21-23], and the effects of geometry [24], materials [25,26], operation conditions [27] on HT-PEMFC have been widely

investigated in the literature. Recently, more and more researchers focused on integrating HT-PEMFC stack with steam reformer [28] or the application of HT-PEMFC stack in CHP [29,30]. The fuel for the HT-PEMFC stack is provided by the reformer which directly converts the natural gas or methanol to H_2-rich reformate gas that usually consists of 65~75 vol% (volume fraction) H_2, 15~25% CO_2, 5~15 vol% H_2O, 1~3 vol% CO, and a trace amount of other impurities [31]. Thus, it is necessary to investigate the effects of reformate gas, especially CO, on HT-PEMFC for using reformate gas as fuel directly. Some previous works have experimentally investigated the effects of CO poisoning at different operation conditions on HT-PEMFC [32-34] and estimated the average coverage of CO and H_2 by the empirical formula. According to their results, increasing the temperature can improve HT-PEMFC performance and CO tolerance. In addition, by comparing the performance of adding the same content of N_2 and CO_2 to pure H_2 (or containing CO) as anode reactants, respectively, the results show that CO_2 only has the effect of diluting hydrogen. This means that CO_2 is hardly converted to CO by water shift reaction within the operating temperature range of HT-PEMFC [35,36]. Zhang et al. [37] determined the optimal working temperature (160~180^{o}C) of HT-PEMFC by weighing the effects of temperature on performance improvement, CO tolerance, durability. Furthermore, A series of up to 1000h durability tests with different anode gas compositions were performed by Pinar et al. [36], demonstrated the feasibility of HT-PEMFC operation with reformate gas. Recently, Yan et al. [19] examined the effects of CO and N_2 concentration, working temperature, and the stoichiometry ratio on a self-made five-cell HT-PEMFC stack. The results indicate that the impedance increases significantly when the concentration of CO increases from 1 vol% to 3 vol%; when the CO concentration further increases to 5 vol%, the increase in impedance is limited. Still, it is difficult to show the distribution of physical variables inside the fuel cell by experiments.

Numerical simulation is a useful and powerful tool for understanding more details about the heat and mass transfer and electrochemical phenomena in PEMFC about CO poisoning, and early works mainly focused on LT-PEMFC [38-41]. For HT-PEMFC, only

a handful of literature about the CO poisoning model has been published. Bergmann [35] developed a 2-D non-isothermal model to investigate dynamic performance. Then, Jiao et al. [42,43] established the first 3-D non-isothermal HT-PEMFC CO poisoning model to study the effects of temperature, CO concentration, and geometry shape of the gas channel on the polarization curve, the CO coverage distribution, the H_2 coverage distribution, and the voltage distribution. This model may be based on the LT-PEMFC CO poisoning model developed in Ref. [44]. Based on the above model developed by Jiao et al. [42], a transient 3-D isothermal anodic electro-kinetic CO poisoning model was established by Raj et al. [45-47] to investigate dynamic response, such as warm-up process at different temperature increase rates, step current operating condition at different extracted current and different CO concentrations. Besides, Oh et al. [48,49] also developed a 3-D non-isothermal CO poisoning model of HT-PEMFC based on the early work of Springer et al. [50] about LT-PEMFC CO poisoning model. The effects of the key kinetic parameters, such as reaction hydrogen adsorption rate, the order kinetics of hydrogen adsorption/desorption processes, on the accuracy of model have been investigated in their research.

1.2. Research Gap and new contribution of this paper

There are several studies about the HT-PEMFC CO poisoning model, but only been verified by experiments in a very narrow range, which does not cover the normal operating range (120~180^{o}C) of HT-PEMFC as well as the possible CO concentration range (1~5 mol% (mole fraction) [34]) in reformate gas. Except that, only a single cell is considered in the previous CO poisoning model. For comprehensively understanding the HT-PEMFC stack CO poisoning, the 3-D HT-PEMFC stack CO poisoning model is needed. Therefore, in the present work, by comparing the results of the single-channel numerical model with the experimental results in Ref. [32], the anodic kinetic parameters are modified, so that the model can predict the impact of CO poisoning in a broad working range. Then, the 3-D numerical models of single-cell stack, three-cell stack and five-cell stack are developed to analyze the influence of CO poisoning on different stacks and

different cells in a stack at 160°C with 3 mol% CO contained in H_2. Finally, the effects of temperature, anode inlet gas composition on the performance, the distribution of H_2 coverage and CO coverage of the three-cell stack are discussed. Fig. 1 displays the multi-perspective analysis process of HT-PEMFC CO poisoning in this paper.

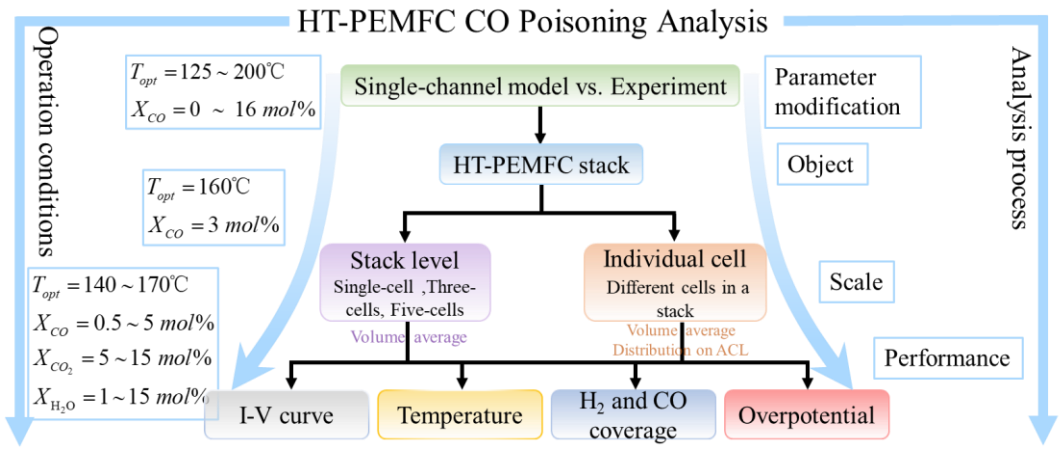

Fig. 1. Schematic of multi-perspective analysis of HT-PEMFC CO poisoning

2. Mathematical model

2.1. Model description and model assumptions

The HT-PEMFC working principle using reformate gas as fuel, the coupling relationship of different physical variables, and the computational domain with mesh configuration of a three-cell stack are shown in Fig. 2. Reactants are transported by convection and diffusion from the gas channel to the gas diffusion layer and then to the catalyst layer where the electrochemical reactions take place. Meanwhile, the products are diffused out from the porous electrode to the gas channel where they are taken away. During the process, variables, such as temperature, current, gas concentration, affect each other, as shown in Fig. 2(b). Fig. 2(c) only depicts the three-cell stack model, as mentioned before. For the single-cell stack model, it can be found in Fig. 3; For the five-cell stack, it has two more cells in the middle than the three-cell stack. Typical components, including bipolar plates (BPs) with gas channels (GCs) and coolant channels (CCs) machined on them, gas diffusion layers (GDLs), catalyst layers (CLs) and the membranes (MEMs) are considered. The cell dimensions, material properties and operating conditions are listed in Table 1.

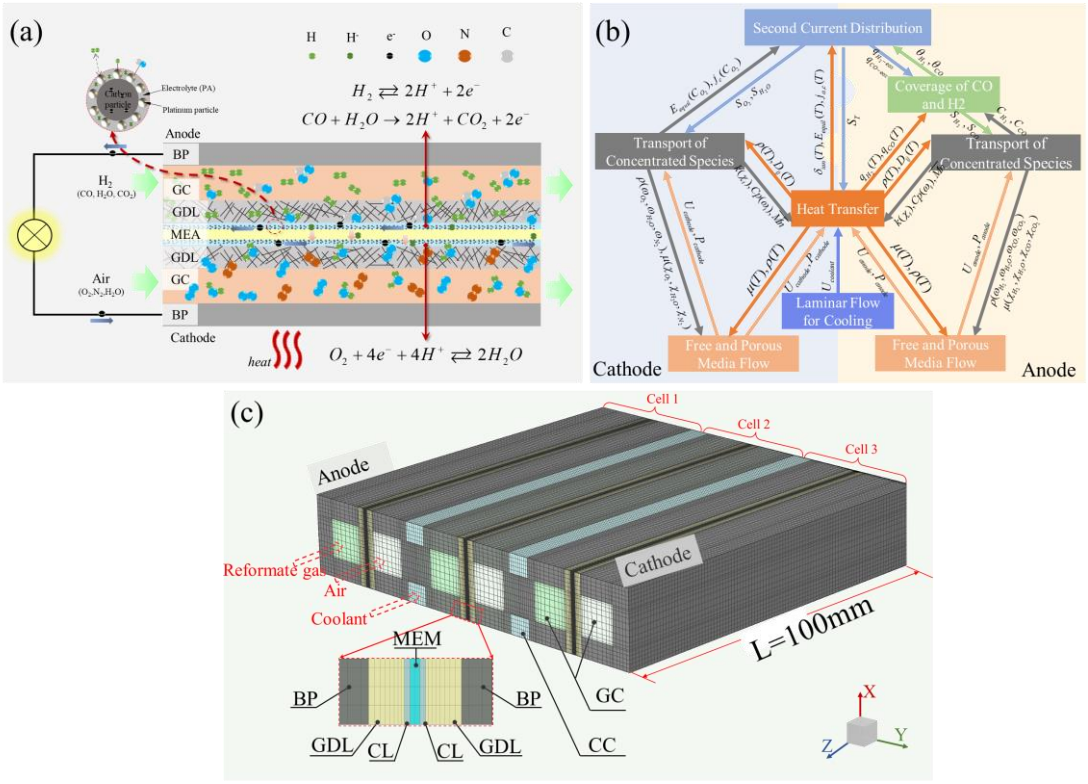

Fig. 2. (a) HT-PEMFC composition and working principle, (b) The coupling relationship between different physical fields, (c) Computational domain and mesh configuration of the three-cell stack.

Before using mathematical formulas to quantitatively describe the physical phenomena that occur inside the HT-PEMFC, there are several assumptions of this numerical model for simplification.

1) Both the anode and cathode gases are considered ideal gases due to low pressure.

2) The flow of both reactant and coolant is laminar due to low velocity.

3) Coolant is considered an incompressible fluid due to low-pressure drop.

4) The properties of GDL and CL are treated as isotropic and homogeneous porous zones with constant porosity and permeability [38].

5) Radiant heat transfer is not considered.

6) The viscous effect of fluid flow results in fluid heating is neglected due to the low velocity and low viscosity.

7) Water produced in the cathode catalyst layer (CCL) is considered to be in the vapor phase due to the high working temperature.

8) The crossover of gas through the membrane is not considered [13].

9) Contact resistance between different components is neglected [13].

Table 1. Stack properties, Operation condition and Species properties [42,48,51-54]

Description	Value
GC length/width/depth; rib width	100/1/1mm; 1mm
Thickness of GDL (TGP-H-060)	0.19mm
Thickness of CL; MEM	0.01mm; 0.05mm
CC width; depth	1mm; 0.6mm
Coolant	FRAGOLTHERM@ S-15-A
Electrical conductivity of CL; GDL; BP	$\kappa_{ele} = 19084; 1250; 14000\, S/m$
Density of CL; GDL; BP; MEM; Coolant	$\rho = 2145; 450; 2266; 1300; 885\ \mathrm{kg/m^3}$
Specific heat capacity of CL; GDL; BP; MEM; Coolant	$C_p = 3300; 568; 1580; 1650; 2290\ \mathrm{J/(kg \cdot K)}$
Thermal conductivity of CL; GDL; BP; MEM; Coolant	$k = 0.95; 1.5; 1.2; 20; 0.158\ \mathrm{W/m{\cdot}K}$
Permeability of CL; GDL	$K = 6.2 \times 10^{-13};\ 6.2 \times 10^{-12}\ \mathrm{m^2}$
Porosity of CL; GDL	$\varepsilon = 0.3;\ 0.78$
Doping Level of PA molecules per PBI repeat unit	$DL = 6.2$
Volume fraction of electrolyte in CL	$\gamma = 0.4$
Stoichiometric ratio	$\zeta_a = 1.2,\ \zeta_c = 2.5$
Reference current density	$I^{ref} = 1.5\mathrm{A/cm^2}$
Inlet velocity of coolant	$U_{coolant} = 0.2\mathrm{m/s}$

Species Transport Parameters	Correlation/Value (T in K, p in Pa)	Unit
Dynamic viscosity	$\mu_{H_2} = 3.205\times10^{-3}\left(T/293.85\right)^{1.5}\left(T+72\right)^{-1}$ $\mu_{O_2} = 8.46\times10^{-3}\left(T/292.25\right)^{1.5}\left(T+127\right)^{-1}$ $\mu_{H_2O} = 7.512\times10^{-3}\left(T/291.15\right)^{1.5}\left(T+120\right)^{-1}$ $\mu_{N_2} = 7.33\times10^{-3}\left(T/300.15\right)^{1.5}\left(T+111\right)^{-1}$ $\mu_{CO} = 6.986\times10^{-3}\left(T/288.15\right)^{1.5}\left(T+118\right)^{-1}$ $\mu_{CO_2} = 7.891\times10^{-3}\left(T/293.15\right)^{1.5}\left(T+240\right)^{-1}$	$kg/(m\cdot s)$
Binary diffusion coefficient	$D_{i-j} = D_{i-j}^{ref}\left(T/403.15\right)^{1.5}\left(101325/p\right)$ $D_{H_2-CO}^{ref} = 1.305\times10^{-4}$ $D_{H_2-H_2O}^{ref} = 1.405\times10^{-4}$ $D_{H_2-CO_2}^{ref} = 1.083\times10^{-4}$ $D_{CO-CO_2}^{ref} = 2.271\times10^{-5}$ $D_{CO-H_2O}^{ref} = 4.48\times10^{-5}$ $D_{H_2O-CO_2}^{ref} = 3.28\times10^{-5}$ $D_{O_2-H_2O}^{ref} = 4.53\times10^{-5}$ $D_{O_2-N_2}^{ref} = 3.45\times10^{-5}$ $D_{N_2-H_2O}^{ref} = 4.48\times10^{-5}$	m^2/s

Specific heat capacity of species	$(C_p)_{H_2}=14283$	$(C_p)_{H_2O(g)}=2014$	$J/(kg\cdot K)$
	$(C_p)_{CO}=1043$	$(C_p)_{CO_2}=840.37$	
	$(C_p)_{N_2}=1040.67$	$(C_p)_{O_2}=919.31$	
Thermal conductivity of species	$k_{H_2}=0.1672$	$k_{H_2O(g)}=0.0261$	$W/(m\cdot K)$
	$k_{CO}=0.025$	$k_{CO_2}=0.0145$	
	$k_{N_2}=0.0242$	$k_{O_2}=0.0246$	

2.2. Anode catalyst layer kinetics

The reaction kinetics within the anode catalyst layer (ACL) considered in the present study account for three reaction steps, namely the adsorption, desorption, and electro-oxidation of H_2 and CO, as shown in Eqs. (1)-(4) [48]. Eq. (4) occurs only when there is vapor in the anode gas.

$$CO+Pt \underset{b_{dc}(\theta_{CO})\times k_{ac}}{\overset{k_{ac}}{\rightleftarrows}} (Pt-CO) \tag{1}$$

$$\mathrm{H_2}+2Pt \underset{b_{dh}\times k_{ah}(\theta_{CO})}{\overset{k_{ah}(\theta_{CO})}{\rightleftarrows}} 2(Pt-H) \tag{2}$$

$$(Pt-H) \xrightarrow{k_{eh}} H^+ + e^- + Pt \tag{3}$$

$$(Pt-CO)+H_2O \xrightarrow{k_{ec}} Pt+CO_2+2H^+ + 2e^- \tag{4}$$

Where the adsorption rate of CO, k_{ac}, the desorption ratio of CO, b_{dc}, the adsorption rate of H_2, k_{ah}, and the desorption ratio of H_2, b_{dh}, can be calculated by the following formulas [46].

$$k_{ac}=k_{ac}^0 \exp(-E_{ac}/RT) \tag{5}$$

$$b_{dc}=b_{dc}^0 \exp\left[\theta_{CO}\cdot\delta(\Delta G_{CO})/RT\right]\cdot\exp(-E_{dc}/RT) \tag{6}$$

$$k_{ah}=k_{ah}^0 \exp\left(\left(-\delta(\Delta E_H)/RT\right)\cdot\left(1-\exp\left(-\lambda\cdot\theta_{CO}/1-\theta_{CO}\right)\right)\right)\cdot\exp(-E_{ah}/RT) \tag{7}$$

$$b_{dh}=b_{dh}^0 \exp(-E_{dh}/RT) \tag{8}$$

$\delta(\Delta G_{CO})$ (J/mol) represents the difference of free energy of CO adsorption between $\theta_{CO}=1$ and $\theta_{CO}=0$. And $\delta(\Delta E_H)$ (J/mol) represents the variation in the activation

energy for hydrogen dissociative adsorption near CO occupied site. λ represents the number of affected sites per CO site for hydrogen adsorption [38]. The electro-oxidation rate of H_2 and CO, k_{eh}, k_{ec} ,can be calculated by Eqs. (9) and (10).

$$k_{eh} = \theta_H \cdot j_H^{ref} \cdot \left(\exp\left(\frac{\alpha_a F \eta_a}{RT} \right) - \exp\left(\frac{-\alpha_c F \eta_a}{RT} \right) \right) \tag{9}$$

$$k_{ec} = \theta_{CO} \cdot j_{CO}^{ref} \cdot \exp\left(\alpha_{CO} F \eta_a / RT \right) \tag{10}$$

θ_H, θ_{CO} represent the fractional coverage of the catalyst sites occupied by hydrogen atoms and CO molecules, respectively. By combination Eqs. (1)-(10) with the balanced equations of the species, θ_H, θ_{CO} can be calculated by Eqs. (11) and (12) [49].

$$\left(\overline{\rho_{pt}} F \right) \frac{d\theta_{CO}}{dt} = k_{ac} P_{co} \theta_{Pt} - b_{dc} k_{ac} \theta_{CO} - k_{ec} = 0 \tag{11}$$

$$\left(\overline{\rho_{pt}} F \right) \frac{d\theta_H}{dt} = 2\left(k_{ah} P_{H_2} \theta_{Pt}{}^2 - b_{dh} k_{ah} \theta_H{}^2 \right) - k_{eh} = 0 \tag{12}$$

In the present study, HT-PEMFC operates at steady-state condition, so the transient term or the time term of Eqs. (11) and (12) are equal to zero. $\overline{\rho_{Pt}}$ $(\mathrm{mol/m^2})$ represents molar area density of catalyst sites [50], P_{CO}, P_{H_2} represent partial pressure of CO and H_2 respectively, and θ_{Pt} stands for unoccupied catalyst sites.

$$\theta_{Pt} = 1 - \theta_H - \theta_{CO} \tag{13}$$

Other reaction kinetic parameters or variables except for $\delta(\Delta G_{CO})$ and $\delta(\Delta E_H)$ are listed in Table 2.

Table 2. Parameters for HT-PEMFC CO poisoning model [32,46,49]

Description	Correlation/Value
CO adsorption rate constant	$k_{ac}^0 = 1.61\times10^4\ \mathrm{A}/\left(\mathrm{Pa\cdot m^2}\right)$
Activation energy for CO adsorption	$E_{ac} = 4.73\times10^4\ \mathrm{J/mol}$
CO desorption rate constant	$b_{dc}^0 = 2.26\times10^{23}\ \mathrm{Pa}$
Activation energy for CO desorption	$E_{dc} = 1.96\times10^5\ \mathrm{J/mol}$

H_2 adsorption rate constant with $\theta_{CO}=0$	$k_{ah}^0=79.85\,\mathrm{A}/\left(\mathrm{Pa}\cdot\mathrm{m}^2\right)$
Activation energy for H_2 adsorption	$E_{ah}=1.04\times10^4\,\mathrm{J/mol}$
H_2 desorption rate constant	$b_{dh}^0=1.51\times10^{15}\mathrm{Pa}$
Activation energy for H_2 desorption	$E_{dh}=8.79\times10^4\,\mathrm{J/mol}$
Number of affected sites per CO site for H_2 adsorption	$\lambda=5$

2.3. Governing equations

As shown in Fig. 2 (b), the model comprehends the conservation of mass, momentum, energy, species, and charges equations to describe physical phenomena in HT-PEMFC. The governing equations and the relevant source/sink terms are listed in Table 3. The electrochemical properties are summarized in Table 4.

Table 3. Governing equations and source/sink terms of HT-PEMFC model

Governing equations		
Mass (GC, GDL, CL, CC)	$\nabla\cdot\left(\rho\vec{u}\right)=S_m$	
Momentum (GC, GDL, CL, CC)	$\frac{\rho}{\varepsilon^2}\left(\vec{u}\cdot\nabla\right)\vec{u}=\nabla\cdot\left[-p\vec{I}+\frac{\mu}{\varepsilon}\left(\nabla\vec{u}+\left(\nabla\vec{u}\right)^T\right)-\frac{2}{3}\frac{\mu}{\varepsilon}\left(\nabla\cdot\vec{u}\right)\right]-\frac{S_m}{\varepsilon^2}\vec{u}+S_u$	
Energy (all domain)	$\left(\rho\mathrm{C}_p\right)^{eff}\vec{u}\cdot\nabla T-\nabla\cdot k^{eff}\nabla T=S_T$	
Species (GC, GDL, CL)	$\rho\left(\vec{u}\cdot\nabla\right)\omega_i=\rho\omega_i\sum_{j=1}^{N}D_{i-j}^{eff}\left(\nabla x_j+\frac{1}{p}\left(\nabla x_j-\omega_j\right)\nabla p\right)+S_i$	
Charges (BP, GDL, CL, MEM)	Electron: $\nabla\left(\kappa_{ele}^{eff}\nabla\varphi_{ele}\right)=S_\varphi$	
	Proton: $\nabla\left(\kappa_{ion}^{eff}\nabla\varphi_{ion}\right)=-S_\varphi$	
Source/Sink terms		**Unit**
$S_m=S_{H_2}+S_{O_2}+S_{H_2O}+S_{CO}+S_{CO_2}$		$kg/\left(m^3\cdot s\right)$
$S_{H_2}=\begin{cases}-\frac{j_H}{2F}M_{H_2}\ (ACL)\\0\quad(other\ zone)\end{cases}$	$S_{O_2}=\begin{cases}0\quad(other\ zone)\\-\frac{j_c}{4F}M_{O_2}\ (CCL)\end{cases}$	
$S_{H_2O}=\begin{cases}-\frac{j_{CO}}{2F}M_{H_2O}\ (ACL)\\\frac{j_c}{4F}M_{H_2O}\quad(CCL)\\0\quad(other\ zone)\end{cases}$	$S_{CO}=\begin{cases}-\frac{j_{CO}}{2F}M_{CO}\ (ACL)\\0\quad(other\ zone)\end{cases}$	$kg/\left(m^3\cdot s\right)$
$S_{CO_2}=-S_{CO}\frac{M_{CO_2}}{M_{CO}}$		

$S_\varphi = \begin{cases} j_a & (ACL) \\ j_c & (CCL) \\ 0 & \text{(other zone)} \end{cases}$	A/m^3
$S_u = \begin{cases} -K\vec{u}/\mu & (CL\ and\ GDL) \\ 0 & (other\ zone) \end{cases}$	$kg/\left(m^2 \cdot s^2\right)$
$S_T = \begin{cases} j_a \lvert\eta_a\rvert + \lVert\nabla\varphi_{ele}\rVert^2 \kappa_{ele}^{eff} + \lVert\nabla\varphi_{ion}\rVert^2 \kappa_{ion}^{eff} & \text{(ACL)} \\ j_c \left(\lvert\eta_c\rvert + \left\lvert T\dfrac{dE_{eq}^c}{dT}\right\rvert \right) + \lVert\nabla\varphi_{ele}\rVert^2 \kappa_{ele}^{eff} + \lVert\nabla\varphi_{ion}\rVert^2 \kappa_{ion}^{eff} & \text{(CCL)} \\ \lVert\nabla\varphi_{ele}\rVert^2 \kappa_{ele}^{eff} & \text{(GDL and BP)} \\ \lVert\nabla\varphi_{ion}\rVert^2 \kappa_{ion}^{eff} & \text{(MEM)} \end{cases}$	W/m^3

229

230

231

232 Table 4. Electrochemical properties for HT-PEMFC [28,55,56]

Description	Correlation/Value (T in K)
Reference exchange current density with $T_{ref} = 353.15K, A/m^2$	$j_H^{ref} = 10^4 \exp[-1400(\frac{1}{T} - \frac{1}{T_{ref}})]$ $j_{O_2}^{ref} = 0.02 \exp[-7900(\frac{1}{T} - \frac{1}{T_{ref}})]$ $j_{CO}^{ref} = 2 \times 10^{-3}$
Transfer current density, A/m^3	$j_H = \theta_H \cdot a \cdot j_H^{ref} \cdot \left(\exp\left(\frac{\alpha_a F \eta_a}{RT} \right) - \exp\left(\frac{-\alpha_c F \eta_a}{RT} \right) \right)$ $j_{O_2} = a \cdot j_{O_2}^{ref} \cdot \left(\frac{C_{O_2}}{C_{O_2}^{ref}} \right)^{0.75} \left(\exp\left(\frac{\alpha_a F \eta_c}{RT} \right) - \exp\left(\frac{-\alpha_c F \eta_c}{RT} \right) \right)$ $j_{CO} = \theta_{CO} \cdot a \cdot j_{CO}^{ref} \cdot \exp\left(\frac{\alpha_{CO} F \eta_a}{RT} \right)$ $j_a = j_H + j_{CO}, \quad j_c = j_{O_2}$
Surface Overpotential, η	$\eta_a = \varphi_{ele} - \varphi_{ion} - E_{eq}^a$ $\eta_c = \varphi_{ele} - \varphi_{ion} - E_{eq}^c$
Equilibrium potential	$E_{eq}^a = 0$ $E_{eq}^c = 1.185\text{-}2.3 \times 10^{-4} \left(T - 298.15 \right) + \frac{RT}{2F} \ln\left(p_{H_2}^{in} \left(p_{O_2}^{in} \right)^{1/2} \right) - E_{loss}$
Open circuit voltage loss	$E_{loss} = 0.17465V$
Transfer coefficients	$\alpha_a = \alpha_c = 0.95, \ \alpha_{CO} = 0.5$
The ratio of reaction surface to CL volume, a, $1/m$	$a = 1 \times 10^5$
Reference O_2 molar concentration,	$C_{O_2}^{ref} = 40.88$

$C_{O_2}^{ref}$,	mol/m^3

2.4. Additional constitutive equations

In the present work, the proton conductivity of membrane is only correlated with temperature and doping level of PA in the PBI membrane [57]:

$$\kappa_{ion} = \frac{100}{T}\exp\left(8.0219 - \frac{2605.6 - 70.1DL}{T}\right) \tag{14}$$

The effective electron conductivity and proton conductivity of CL are corrected by using Bruggeman correlation to combine the effects of porosity (ε) and electrolyte volume fraction (γ) in the CL [27]:

$$\kappa_{ele}^{eff} = \left(1-\varepsilon-\gamma\right)^{1.5}\kappa_{ele} \tag{15}$$

$$\kappa_{ion}^{eff} = \gamma^{1.5}\kappa_{ion} \tag{16}$$

As mentioned before, the gases at both anode and cathode are assumed as ideal gases. Thus, the density of the gas mixture is calculated based on the ideal gas law [27]:

$$\rho = p\left(RT\sum_{i}^{N}\frac{\omega_i}{M_i}\right)^{-1} \tag{17}$$

The dynamic viscosity and the thermal conductivity of the gas mixture can be calculated based on the kinetic theory [58]:

$$\psi_m = \sum_{i=1}^{N}\frac{x_i\psi_i}{\sum_{j=1}^{N}x_j\phi_{ij}} \tag{18}$$

$$\phi_{ij} = \frac{\left[1+\left(\psi_i/\psi_j\right)^{1/2}\left(M_j/M_i\right)^{1/4}\right]^2}{\left[8\left(1+M_j/M_i\right)\right]^{1/2}} \tag{19}$$

Where ψ_m, ψ_i, ψ_j represent the dynamic viscosity or the thermal conductivity of the

mixture gas, $i\text{-}th$, $j\text{-}th$ species, respectively. And x_i is mole fraction of species i.

The specific heat capacity of the gas mixture is determined by the mass fraction of each species [53]:

$$C_p = \sum_{i=1}^{N} \omega_i \left(C_p\right)_i \tag{20}$$

For the porous region (CL, GDL), the effective volumetric heat capacity and the effective thermal conductivity are based on the volume average formula [53]:

$$\begin{aligned} \left(\rho C_p\right)_{cl}^{eff} &= \varepsilon \rho_g C_{p,g} + \gamma \rho_{mem} C_{p,mem} + \left(1\text{-}\varepsilon\text{-}\gamma\right) \rho_{cl} C_{p,cl} \quad \text{(CL)} \\ \left(\rho C_p\right)_{gdl}^{eff} &= \varepsilon \rho_g C_{p,g} + \left(1\text{-}\varepsilon\right) \rho_{gdl} C_{p,gdl} \qquad \text{(GDL)} \end{aligned} \tag{21}$$

$$\begin{aligned} k_{cl}^{eff} &= \varepsilon k_g + \gamma k_{mem} + \left(1\text{-}\varepsilon\text{-}\gamma\right) k_{cl} \quad \text{(CL)} \\ k_{gdl}^{eff} &= \varepsilon k_g + \left(1\text{-}\varepsilon\right) k_{gdl} \qquad \text{(GDL)} \end{aligned} \tag{22}$$

The effective binary diffusion coefficient in the porous regions (CL, GDL) are modified by the Bruggeman correlation [53]:

$$D_{i\text{-}j}^{eff} = \varepsilon^{1.5} D_{i-j} \tag{23}$$

2.5. Boundary conditions

At the inlet of gas channels (GCs) and coolant channels (CCs), the fully developed flow is used, and the inlet velocity of GCs is determined by reference current density, the stoichiometric ratio, as well as the inlet molar concentration. The outlet of GCs and CCs is set at 1*atm* (absolute pressure). When calculating the inlet velocity of GCs, the inlet pressure is assumed to be equal to the outlet pressure due to a small pressure drop, and the temperature is assumed as operation temperature [59].

$$U_{a,in} = \frac{\zeta_a I^{ref} A_{cl} R T_{a,in}}{2F A_{a,in} x_{H_2,in} p_{a,in}}, \; U_{c,in} = \frac{\zeta_c I^{ref} A_{cl} R T_{c,in}}{4F A_{c,in} x_{O_2,in} p_{c,in}} \tag{24}$$

Where A_{cl}, A_{in} represent the flat active surface area of the CL and cross-sectional inlet area of the GC.

As for the boundary conditions for the electrochemical model, at the anode side of the HT-PEMFC stack, the potential is set to zero. And at the cathode side, the potential is determined by operation voltage.

Thermal boundary condition specified on the end surface of BP is $T_{BP} = T_{opt}$. Heat flux is specified at the GCs inlet and CCs inlet, which can be calculated by the following equation [53]:

$$q = \rho \vec{u} \left[\int_{T_{in}}^{T} C_p dT + \int_{p_{in}}^{p} \frac{1}{\rho} (1 - \chi T) dp \right] \tag{25}$$

Where χ (1/K) represents the coefficient of thermal expansion, for ideal gas, $\chi = 1/T$; for liquid, $\chi = 1$.

Symmetrical boundary conditions and no-slip boundary conditions are applied on the side surfaces normal to X-axis.

2.6. Numerical implementation

The governing equations listed in Table 3 and H_2 and CO coverage Eqs. (11)-(12) are discretized and solved in the commercial software COMOSL Multiphysics based on the finite element method (FEM). The Segregated algorithm is applied to solve the discrete equation, which reduces the need for computing power and allows different solvers to be selected for different equations. MUMPS solver is used for conservation equation of current as well as H_2 and CO coverage equation, and PARDISO solver is used for energy conservation equation, and Algebraic Multigrid solver is used for the rest conservation equations. To improve convergence, firstly, the primary current distribution is used for

initialization; Then, solve different physical fields separately; Finally, the results of previous steps are substituted into the fully coupled calculation as the initial value. The relative tolerance for all variables is set to $1e^{-5}$. The total number of computational elements are 160000, 504000, 848000 for single-cell stack, three-cell stack, and five-cell stack, respectively. The mesh parameters are the same for different stacks.

3. Results and discussion

3.1. Model validation

There are two aims for model validation, one is to examine the accuracy of the model, the other is to calibrate some parameters, such as $\delta(\Delta G_{CO})$ and $\delta(\Delta E_H)$. The experimental data are obtained from Ref. [32]. There are several reasons for choosing this data: 1) All the material properties and operating conditions of the cell were given; 2) The working area of CL was $10cm^2$, and the flow rate for hydrogen (or its mixture) and pure oxygen was 270ml/min, so reactants concentration was enough and temperature distribution was uniform. Thus, the single-channel model (single-cell stack model), as shown in Fig.3 (a), is valid for model validation and parameters correction; 3) The normal working temperature range of HT-PEMFC and the possible CO concentration range in reformate gas were covered in the experiment. The comparison between experimental results and simulation results is shown in Fig. 3 (b), indicating the model has reasonable accuracy. The cell properties and working conditions are the same as the experiment in Ref.[32] rather than the parameters in Table 1. Pure oxygen and hydrogen (or its mixture) without humidification at atmospheric pressure (absolute pressure) are used, and the DL for the 65μm thickness membrane is 5.3, and the thickness of GDL (TGP-H-120) is 0.37mm. According to previous research about LT-PEMFC CO poisoning model [38-40], the two parameters, $\delta(\Delta G_{CO})$ and $\delta(\Delta E_H)$, have a strong correlation with temperature and CO mole fraction. Thus, these two parameters have been corrected by temperature and CO mole fraction, as shown in Fig. 3 (c), so that they can be used in HT-PEMFC CO poisoning model.

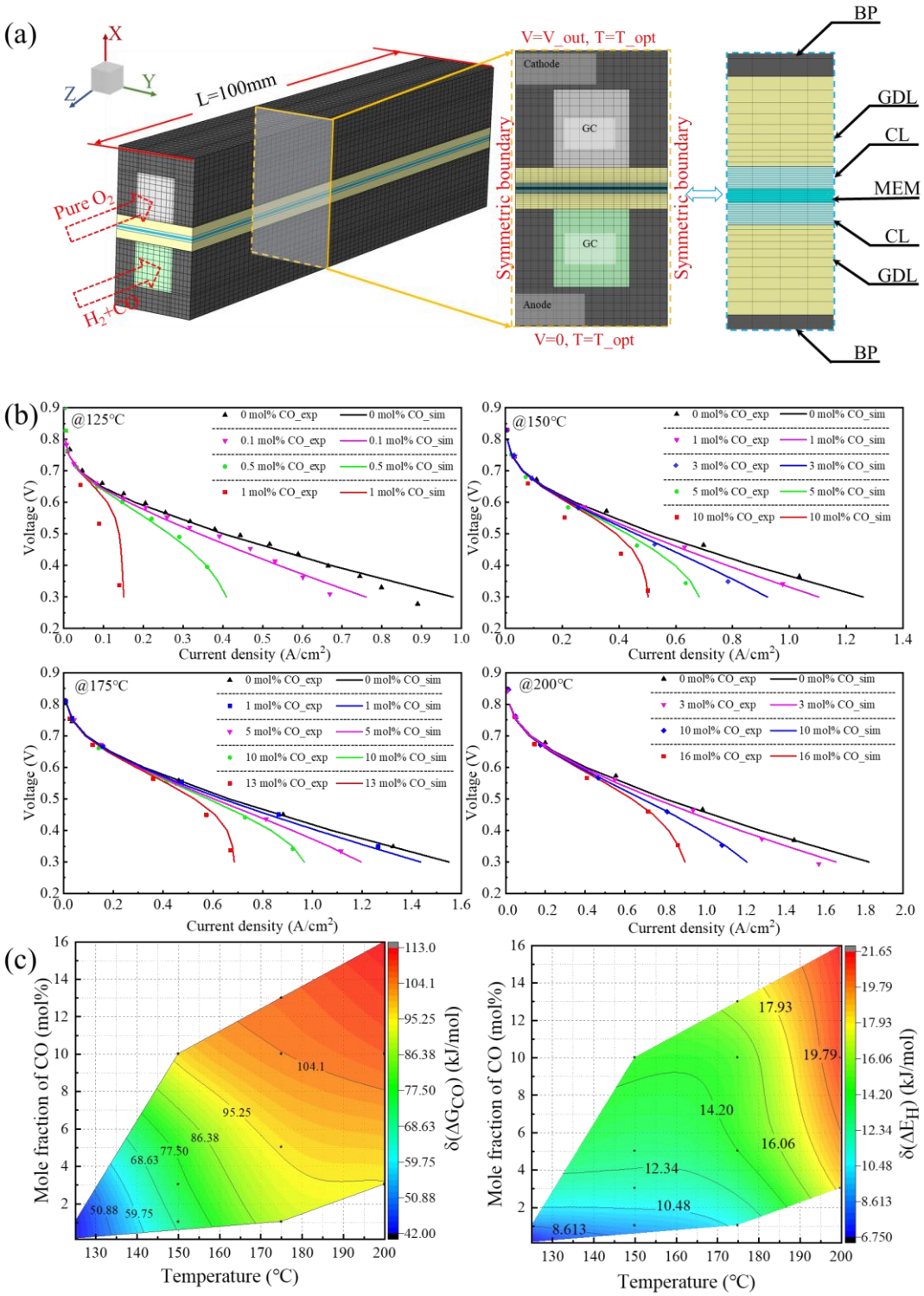

Fig. 3. Model validation. (a) Single-channel model for model validation, (b) The comparison between experimental results and simulation results at different temperatures and different CO mole fractions, (c) $\delta(\Delta G_{CO})$ and $\delta(\Delta E_H)$ change with temperature and CO mole fraction.

3.2. Comparison of stacks with different numbers of cells

Fig. 4 shows the comparison of different stacks at 160ºC and 3 mol% CO contained in H_2. It can be noticed that the volume average temperature of the membrane electrode assembly (MEA=MEM+ACL+CCL) almost linearly increases with current density due to the electrochemical heat produced on MEA. And the stack with more individual cells, the temperature increases more quickly with current density. However, the H_2 coverage decreases with increasing current density. This is because as the current density increases, more hydrogen atoms adsorbed on Pt-sites are required to participate in the electrochemical reaction to provide more protons. Thus, there are more Pt-free sites available for CO adsorption. In the meantime, according to the thermodynamic analysis of CO adsorption on Pt, this procedure is associated with high negative entropy [32,33]. Therefore, the CO coverage first increased slightly and then rapidly decreased. It also can be noticed that the CO coverage of the five-cell stack increases at the slowest rate first, then decreases at the fastest rate. This is because the average MEA temperature of the five-cell stack is the highest at the same current density, making the ability of CO adsorption the weakest. The maximum value of CO coverage is 0.371 at 0.498A/cm^2, 0.366 at 0.230A/cm^2, 0.364 at 0.149A/cm^2 for single-cell stack, three-cell stack, and five-cell stack, respectively. Due to the decrease of CO coverage, the decrease rate of H_2 coverage is reduced with increasing current density. At the same current density, the H_2 coverage of the stack with more individual cells is higher because of lower CO coverage. It can be seen from Fig. 4 (c) that the average output performance of the five-cell stack is the best at the same CO concentration and working temperature which indicates that the multi-cell stack has higher CO tolerance. For an average voltage of 0.3V, the power density of an individual cell in single-cell stack, three-cell stack, and five-cell stack are 0.340, 0.363, 0.374 W/cm^2, respectively. This is because higher internal temperature leads to higher H_2 coverage and lower CO coverage, as shown in Fig. 4 (b), and promotes the electrochemical reaction at CL and the conductivity of the membrane.

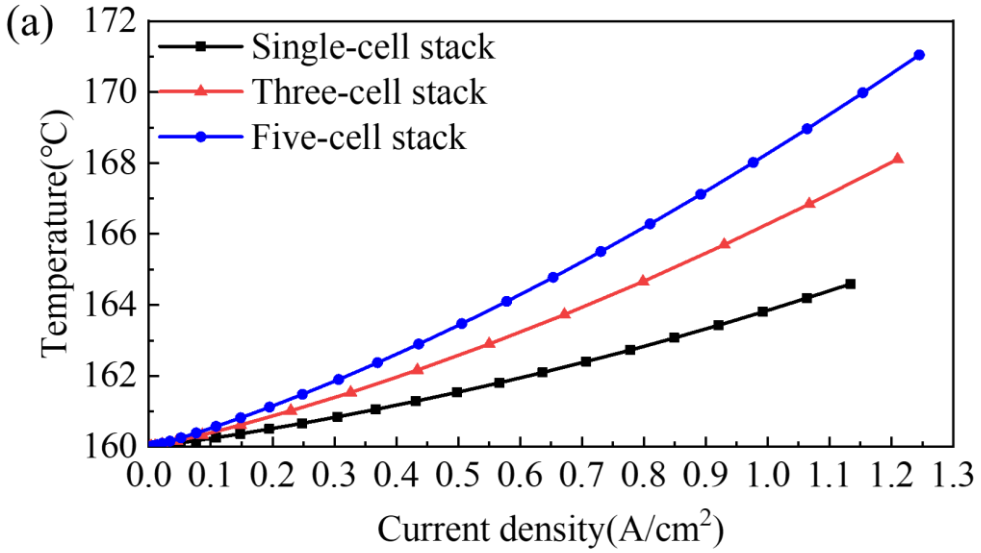
(a)
Single-cell stack
Three-cell stack
Five-cell stack
Temperature(°C)
Current density(A/cm²)

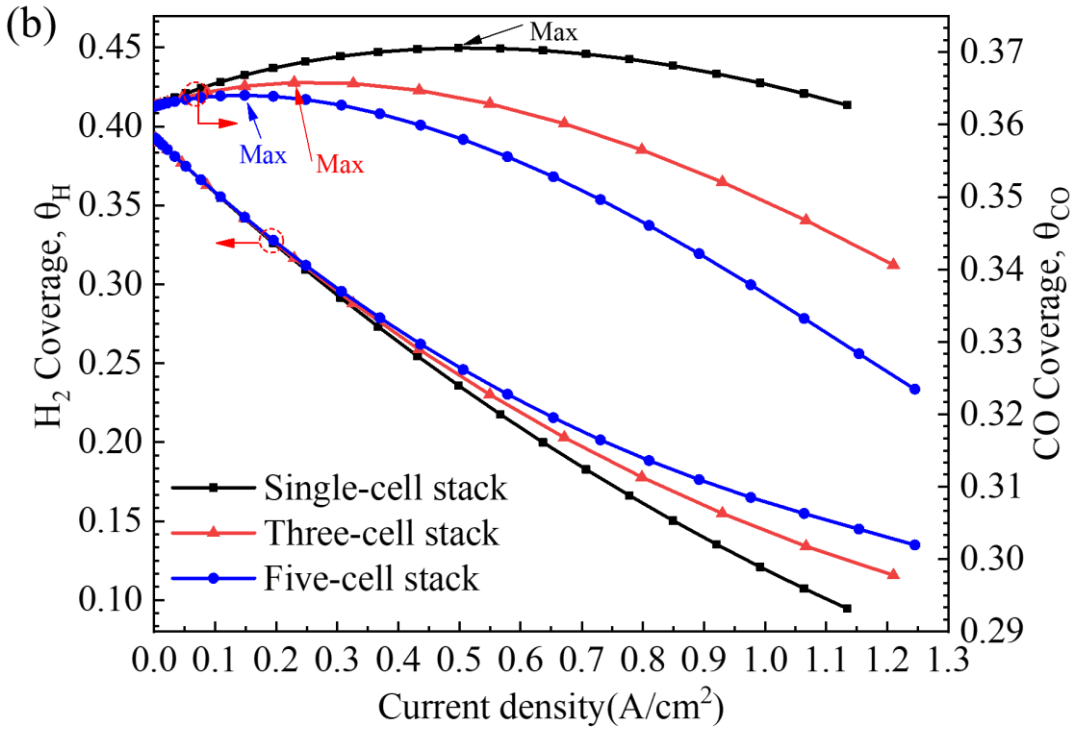
(b)
Max
Max
Max
Single-cell stack
Three-cell stack
Five-cell stack
H₂ Coverage, θH
CO Coverage, θCO
Current density(A/cm²)

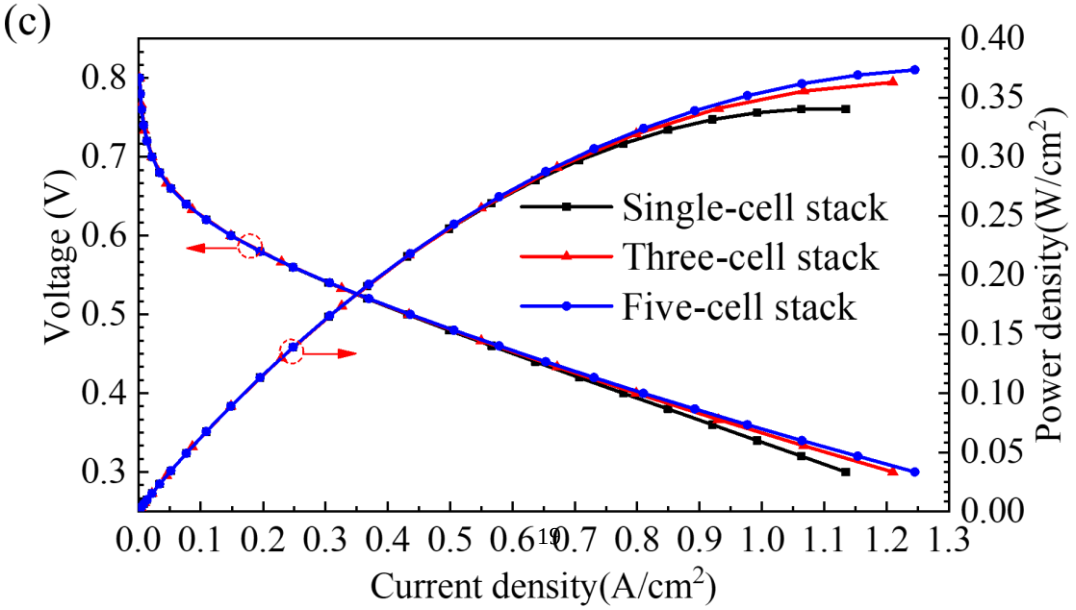
(c)
Single-cell stack
Three-cell stack
Five-cell stack
Voltage (V)
Power density(W/cm²)
Current density(A/cm²)

Fig. 4. Comparison of stacks with different numbers of cells at 160°C and 3 mol% CO contained in H_2. (a) Volume average temperature on MEA, (b) Volume average H_2 and CO coverage fractions on ACL, (c) Polarization curve.

Since the middle-cell is more representative for large practical HT-PEMFC stack with many individual cells [60], the distribution of temperature, H_2 coverage, CO coverage and overpotential over the middle-plane of the ACL of middle-cell of different stacks are depicted in Fig. 5. It can be found that the distribution of these variables is similar for the same individual cell. In general, high temperature corresponds to high H_2 coverage, low CO coverage and low overpotential. However, too high temperature reduces the H_2 coverage and increases the overpotential, as shown in Fig. 5 (c). This is because the increase in temperature can promote hydrogen oxidation reaction (HOR), resulting in more hydrogen atoms adsorbed on Pt being consumed. By comparing Fig. 5 (b) and (c), at a temperature between 175°C and 180°C, the H_2 coverage first increases with increasing temperature, then decreases with a further increase in temperature. Besides, it also can be noticed that the temperature and H_2 coverage under the gas channel are higher than that under the rib, but the CO coverage and overpotential are opposite – higher under the rib [42]. This is because H_2 easily diffuses to the reaction sites in ACL under gas channels and low gas flow velocity under the ribs leads to the accumulation of CO under it. According to the maximum value of H_2 coverage shown in the legend, it can be found that the maximum H_2 coverage of the three-cell stack is higher than that of the five-cell stack and the single-cell stack. The reason is as follows. For the single-cell stack, the maximum temperature is 166.63°C, which is about 10°C lower than that of the three-cell stack, and is about 13°C lower than that of the five-cell stack. Thus, the single-cell stack has the strongest CO adsorption ability, leading to the highest CO coverage. For the five-cell stack, too high temperature promotes the electrochemical reaction, consuming more hydrogen atoms through HOR.

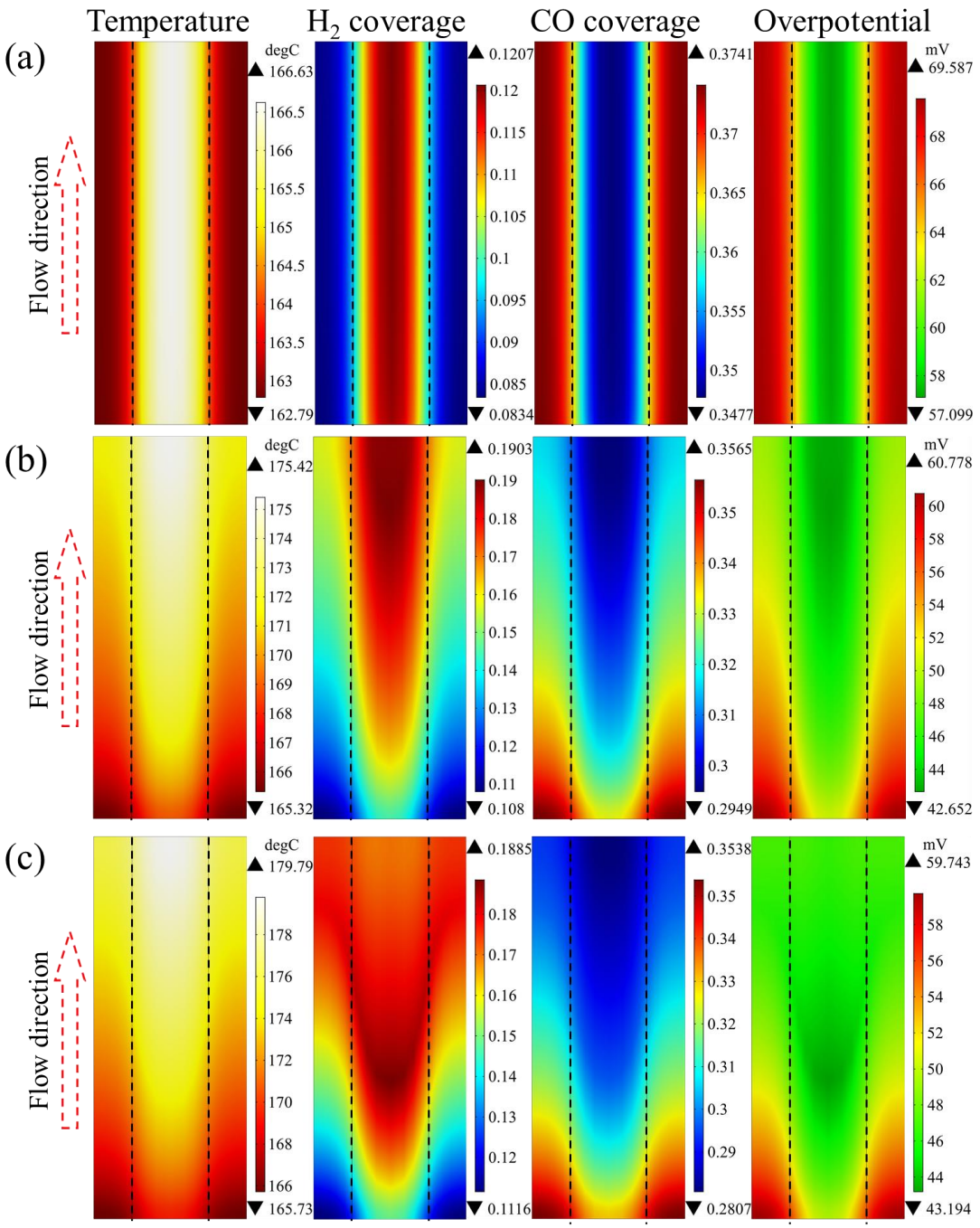

Fig. 5. Distribution of temperature, H_2 coverage, CO coverage and overpotential over the middle of the ACL of the middle-cell of different stacks at an average voltage of 0.3V. (a) Single-cell stack, (b) Three-cell stack, (c) Five-cell stack.

3.3. Comparison of different cells in the stack

For a multi-cell stack, the individual cell on the anode side is defined as Cell 1 and the one on the cathode side is defined as Cell N (N represents the number of cells in a stack),

as demonstrated in Fig. 2 (c). The comparison of polarization curve, H_2 coverage, CO coverage and MEA temperature between different cells in the three-cell stack and the five-cell stack are shown in Fig. 6. It can be seen that the individual cell in the middle has the best performance. And the performance of middle cells (Cell 2 ~ Cell (N-1)) is relatively close, higher than that of Cell 1 and Cell N. The performance of cells at the anode side, namely Cell 1, is poor than that at the cathode side, namely Cell N, which is similar to the experimental results in Ref. [19]. This is because the MEA temperature of Cell N is higher than that of Cell 1, as demonstrated in Fig. 6 (c) and (f), and higher H_2 coverage and lower CO coverage, as shown in Fig. 6 (b) and (e). At an average voltage of 0.3V, the power density of Cell 2 in the three-cell stack is 0.375W/cm^2, 5.6% higher than that of Cell 1. For the five-cell stack, the power density of Cell 3 is 0.385W/cm^2 at 0.3V, 7.8% higher than that of Cell 1. The performance of Cell 2 in the three-cell stack and Cell 3 in the five-cell stack is 9.33%, 11.69% respectively higher than that of the single-cell stack at an average voltage of 0.3V. However, the output power of different cells in a stack has no significant difference when the current density is lower than 0.6A/cm^2 or the average voltage is higher than 0.45V.

The H_2 coverage and CO coverage of different individual cells in a stack varying with current density have similar trends, as shown in Fig. 6 (b) and (e). The cell closer to the middle shows lower volume average CO coverage and higher volume average H_2 coverage. All cells in a stack are connected in series, so the average current density for different cells is the same [60]. Therefore, the total number of hydrogen atoms of each cell participating in the electrochemical reaction is the same. However, due to the difference in temperature distribution, as shown in Fig.6 (c) and (f), different cells have different adsorption and desorption rate of H_2 and CO, which makes the coverage of H_2 and CO in different cells different. It also can be found that the difference of H_2 coverage, CO coverage and MEA temperature between different cells in a stack increases with the increase of current density. When the average voltage is 0.3V, for the three-cell stack, the H_2 coverage of Cell 2 is 0.149, 26.17% higher than that of Cell 1, while for the CO coverage of Cell 2 is 0.320, 6.96% lower than that of Cell 1. For the five-cell stack, the

H_2 coverage of Cell 3 is 0.157, 31.74% higher than that of Cell 1, while for the CO coverage of Cell 3 is 0.307, 10.13% lower than that of Cell 1. The H_2 coverage of Cell 2 of the three-cell stack and Cell 3 of the five-cell stack is 36.30%, 39.87% higher than that of the single-cell stack, respectively, and the CO coverage is 11.65%, 15.36% lower than that of the single-cell stack, respectively.

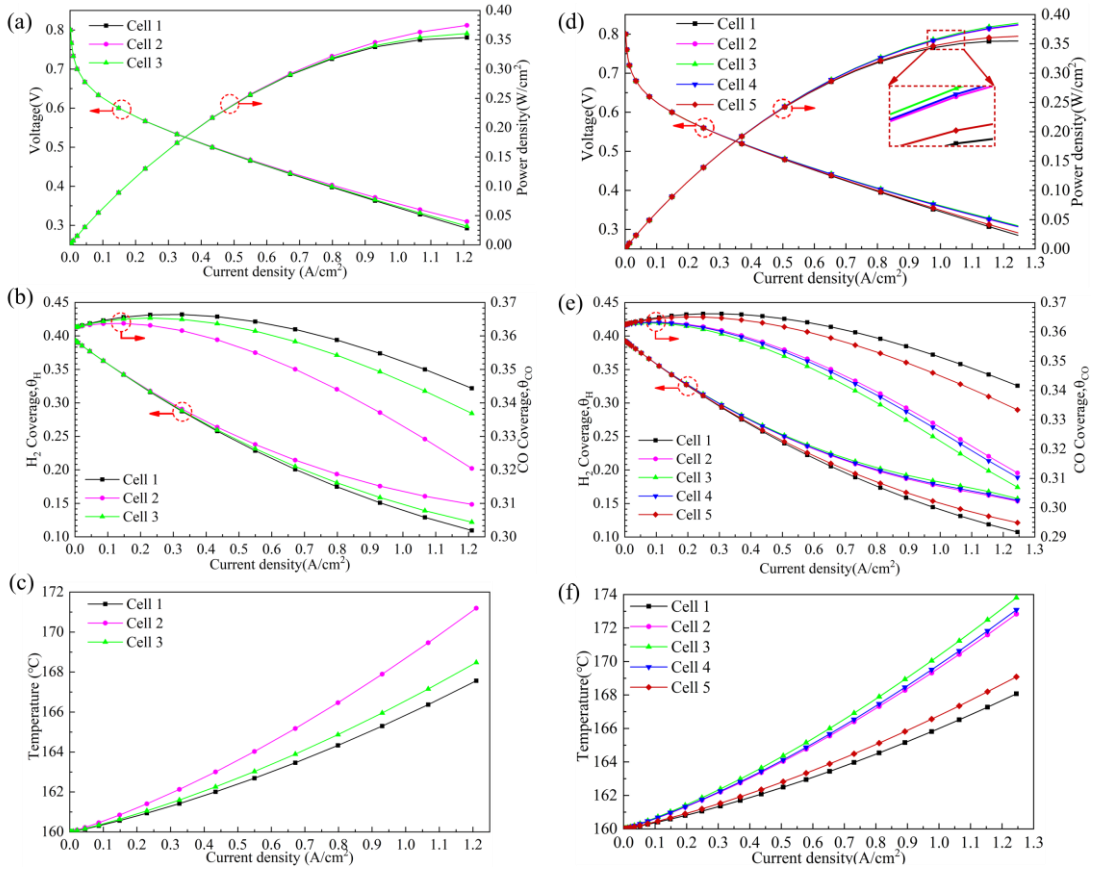

Fig. 6. Comparison between different cells in multi-cell stacks at 160ºC and 3 mol% CO contained in H_2. (a)-(c) Three-cell stack, (d)-(f) Five-cell stack. (a) and (d) Polarization curve, (b) and (e) Volume average H_2 coverage and volume average CO coverage on ACL, (c) and (f) Volume average temperature on MEA.

The temperature distribution of different stacks along the gas channel at mid-plane (Z-Y plane) and the temperature variations along Y direction at Z=50mm on such plane are shown in Fig. 7. It can be found that, as the number of individual cells contained in the stack increases, the temperature distribution becomes more uneven and the temperature

448 difference increases. Thus, for more even temperature distribution of multi-cell stack, the
449 design of the coolant channel is very important. In the present study, counter coolant flow
450 (along the positive Z direction) is also simulated. The result (not presented in the
451 manuscript) shows counter coolant flow alleviates uneven temperature distribution to
452 some extent. Both for the three-cell stack and the five-cell stack, the difference between
453 maximum temperature and minimum temperature reduces almost 1^{o}C. Since the
454 conductivity of MEM is several orders of magnitude lower than the rest parts, and the
455 overpotential at CCL is higher than that at ACL, as well as the cathode has one more heat
456 source term about reaction heat, thus, the highest temperature of each cell appears at CCL,
457 and the highest temperature of a stack appears at the CCL of the middle-cell, as shown in
458 Fig. 7 (b) [13,53]. The MEM in the middle of a multi-cell stack is more likely to fail due
459 to the higher temperature, which causes phosphoric acid (H_3PO_4) to be more easily
460 dehydrated into pyro-phosphoric acid ($H_4P_2O_7$) [31]. The results shown in Fig. 7 indicate
461 that although the temperature distribution on both sides of *Y=0* (MEM of the middle cell)
462 is slightly different, the temperature distribution has good symmetry with respect to *Y=0*.
463 The maximum temperature difference between the right side of *Y=0*, namely close to the
464 cathode side, and the counterpart coordinate at the left side of *Y=0* is about 2.5^{o}C.

465

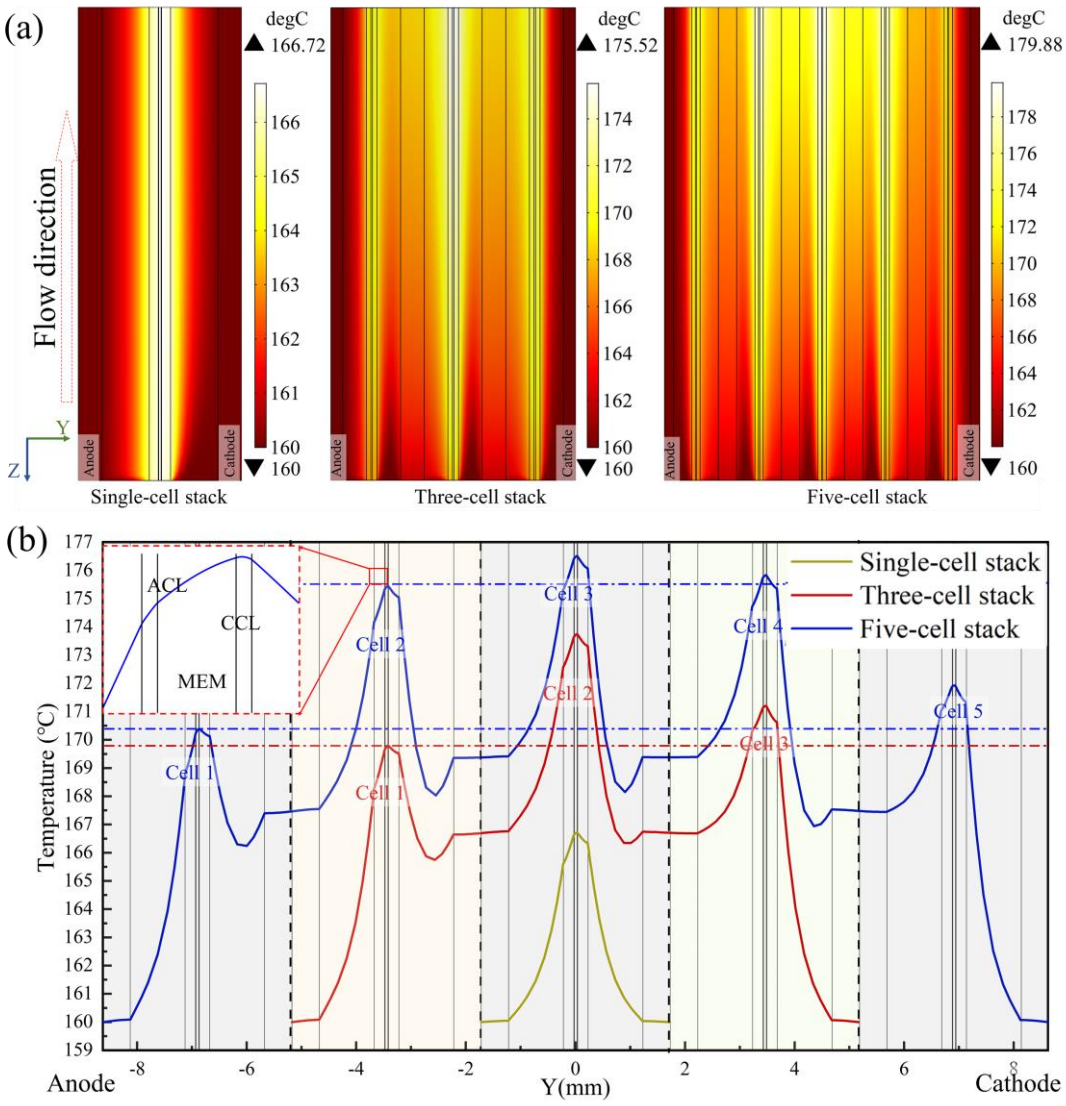

Fig. 7. Temperature distribution of stacks at an average voltage of 0.3V. (a) Along the gas channel at the middle plane (*Z*-*Y* plane), (b) Along the thickness direction of the stack (*Z*=*50mm, Y* direction).

Fig. 8 displays the temperature distribution, the H_2 coverage distribution and the CO coverage distribution of different cells in a stack at an average voltage of 0.3V. The description of the same phenomena that occur in Fig. 5 will not be repeated here. According to the color distribution of contour, it can be observed that the cell closer to the middle shows higher H_2 coverage and lower CO coverage due to higher temperature, and the cell on the anode side (Cell 1) shows lower temperature than the cell on the cathode side (Cell N), which agree with the results shown in Fig. 6 and Fig. 7. Due to

similar temperature distribution and close temperature value, which can also be found in Fig. 7 (b), the H_2 coverage distribution and the CO coverage distribution of Cell 2~Cell 4 of the five-cell stack are almost the same. The distribution of these variables in Cell 1 of the three-cell stack and Cell 1 of the five-cell stack is almost the same, and in Cell 3 of the three-cell stack and Cell 5 of the five-cell stack is almost the same.

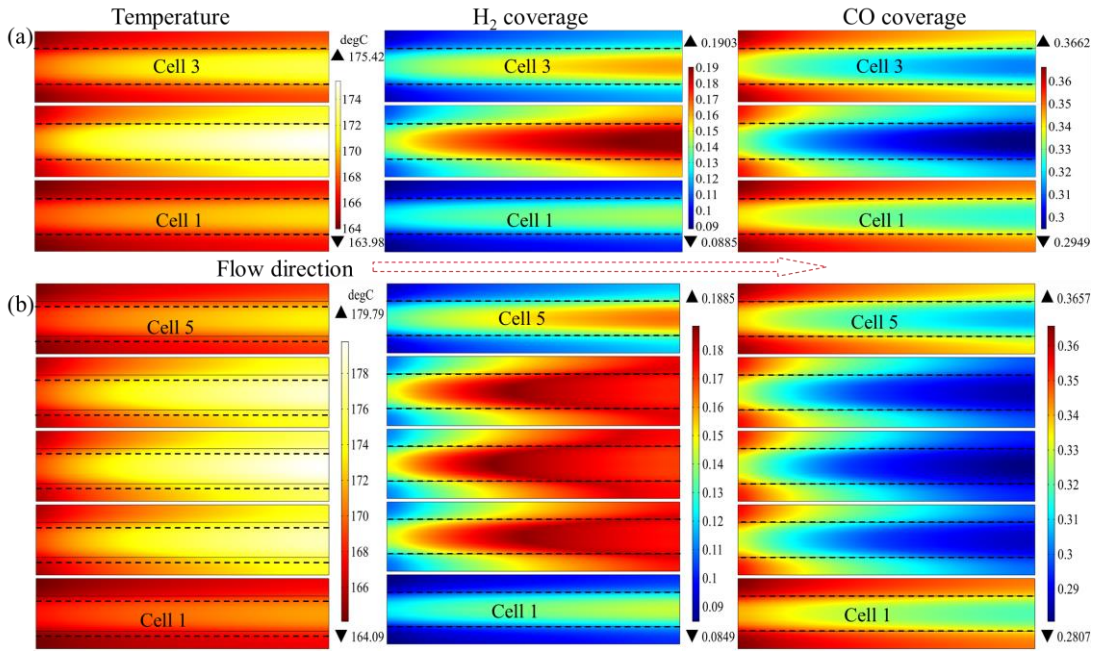

Fig.8. Comparison of temperature, H_2 coverage and CO coverage distribution over the middle of the ACL of different cells in the stack at an average voltage of 0.3V. (a) Three-cell stack, (b) Five-cell stack.

3.4. Effect of operation conditions

Fig. 9 shows the influence of operating temperature and CO mole fraction (mol%) on the performance of the three-cell stack. As expected, increasing operation temperature can improve the performance of HT-PEMFC, and can increase the resistance to CO poisoning [32,42]. When the average voltage is 0.3V and without CO contains in H_2, the current density increases from 1.268A/cm^2 at 140^{o}C, to 1.377A/cm^2 at 150^{o}C, to 1.484A/cm^2 at 160^{o}C, and to 1.588A/cm^2 at 170^{o}C. When the operating temperature is 140^{o}C and the mole fraction of CO increases from 0 to 3 mol%, the current density reduces by 60% at an average voltage of 0.3V. When the mole fraction of CO increases from 0 to 5 mol%,

498 the current density reduces by 62.6%, 49.2%, 38.9% for the operating temperatures of
499 150ºC, 160ºC, 170ºC, respectively. This significant performance degradation is due to the
500 occupation of many Pt-sites by CO, as illustrated in Fig. 10. At an average voltage of
501 0.3V, when operating at 140ºC with 3 mol% CO content or operating at 150ºC to 170ºC
502 with 5 mol% CO content, the H_2 coverage is almost zero. It can also be noticed that when
503 the operating temperature is up to 170ºC, the H_2 coverage and the CO coverage almost
504 decrease linearly with the current density. This is because higher temperature increases
505 the electrochemical oxidation of hydrogen atoms and makes a faster desorption rate of
506 CO at the same time.
507

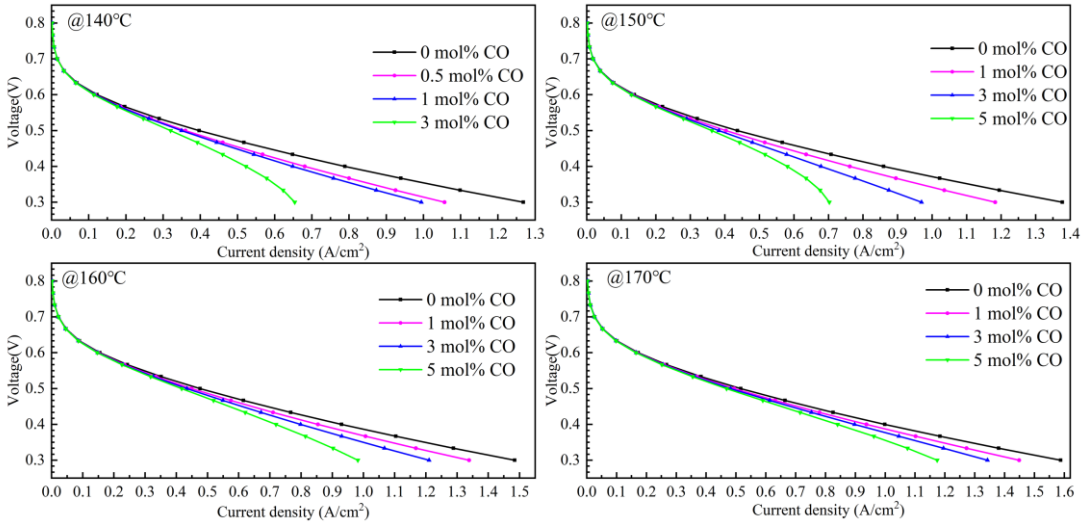

508

509 Fig. 9. Influence of operation temperature and mole fraction of CO on the performance
510 of the three-cell stack.
511

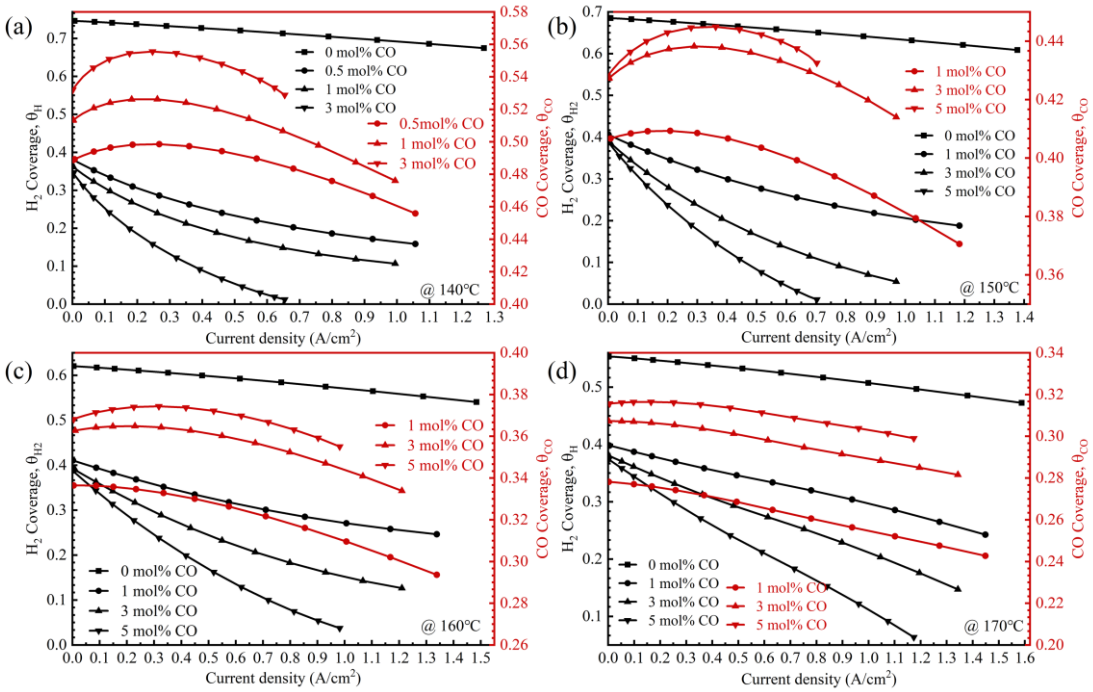

Fig. 10. Influence of operating temperature and mole fraction of CO on the volume average H_2 coverage and the volume average CO coverage at ACL of the three-cell stack.

The influences of the mole fraction of CO_2 and H_2O on the performance, the volume average H_2 coverage, and the volume average CO coverage of the three-cell stack at 160°C are depicted in Fig. 11. As expected, with the increase of mole fraction of CO_2 and H_2O, the performance decreases gradually. When the mole fraction of CO_2 increases from 5 mol% to 20 mol%, the power density at an average voltage of 0.3V reduces by 5.40%, and when the mole fraction of H_2O increases from 1 mol% to 15 mol%, the power density reduces by 6.98%. According to Equation 4, adding a certain amount of water can alleviate CO poisoning. However, the rate of reaction kinetics is very slow at the operating temperature range of HT-PEMFCs, several orders of magnitude lower than the oxygen reduction reaction [35,42]. So, when 1 mol% H_2O is added to 3 mol% CO+10 mol% CO_2, the power density of the three-cell stack reduces by 0.374% at an average voltage of 0.3V. According to Fig. 11 (c) and (d), it also can be found that the H_2 coverage decreases and the CO coverage increases when the mole fractions of CO_2 and H_2O increase. This is because increasing the mole fraction of CO_2 and H_2O decreases the mole fraction of H_2, while the mole fraction of CO is mostly unchanged. Consequently, the adsorption rate of

H_2 is slowed down according to Equations (11) and (12), leaving more Pt-sites for CO adsorption. In addition, with the increase of the current density, the influence of the mole fraction of CO_2 and H_2O on H_2 coverage increases, which is due to the rapid consumption of hydrogen atoms under high current density and the decrease of adsorption rate caused by low hydrogen concentration, and is opposite for the influence on CO coverage which is due to the decrease of adsorption rate caused by the high internal temperature.

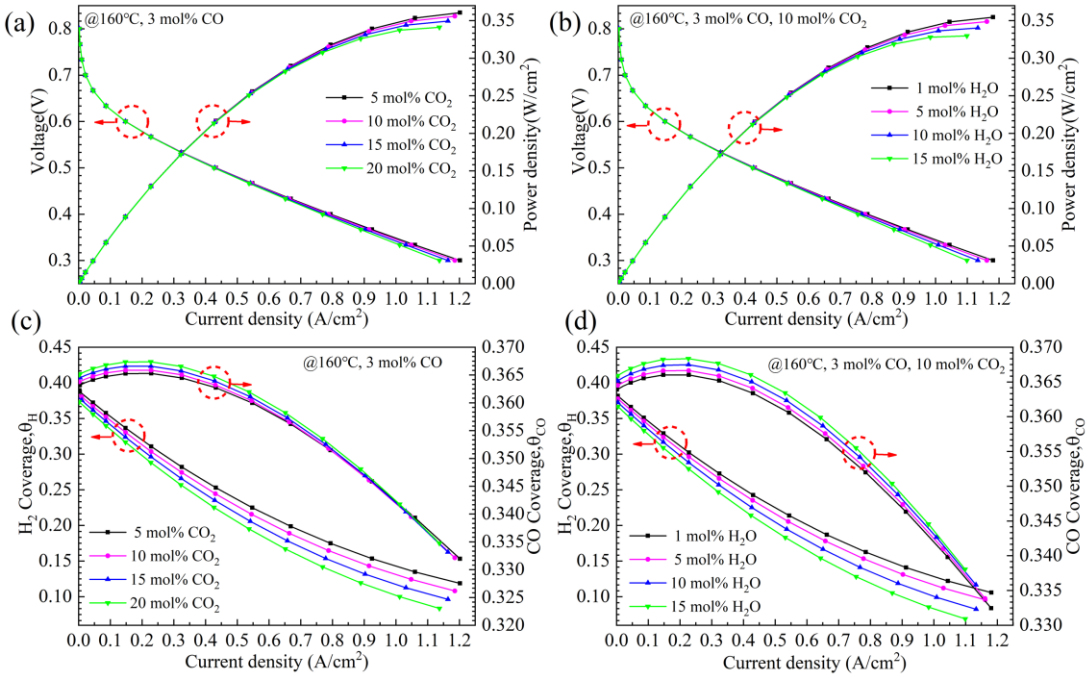

Fig. 11. Influence of mole fraction of CO_2 and H_2O on the three-cell stack. (a) and (b) The performance, (c) and (d) The volume average CO coverage and the volume average H_2 coverage.

The distribution of H_2 coverage and CO coverage over the middle-plane of ACL of the middle-cell at an average voltage of 0.3V under different operation conditions are displayed in Fig. 12. The distribution trend of CO coverage is almost the same, showing a U-shaped distribution, with the lowest value appearing below the outlet of the gas channel [42]. For the H_2 coverage, the distribution varies under different operating conditions. When the operating temperature is 170°C, the H_2 coverage at the outlet of the gas channel is lower than that at the inlet of the gas channel. And when the operating

temperature is 160ºC with 1 mol% CO contained in H_2, the maximum value of H_2 coverage appears in the middle of ACL rather than the outlet. The variation in the distribution of H_2 coverage under different operation conditions is mainly due to the existence of a turning point of hydrogen coverage varies with temperature between 175°C and 180°C, which has been proposed in the analysis of Fig. 5.

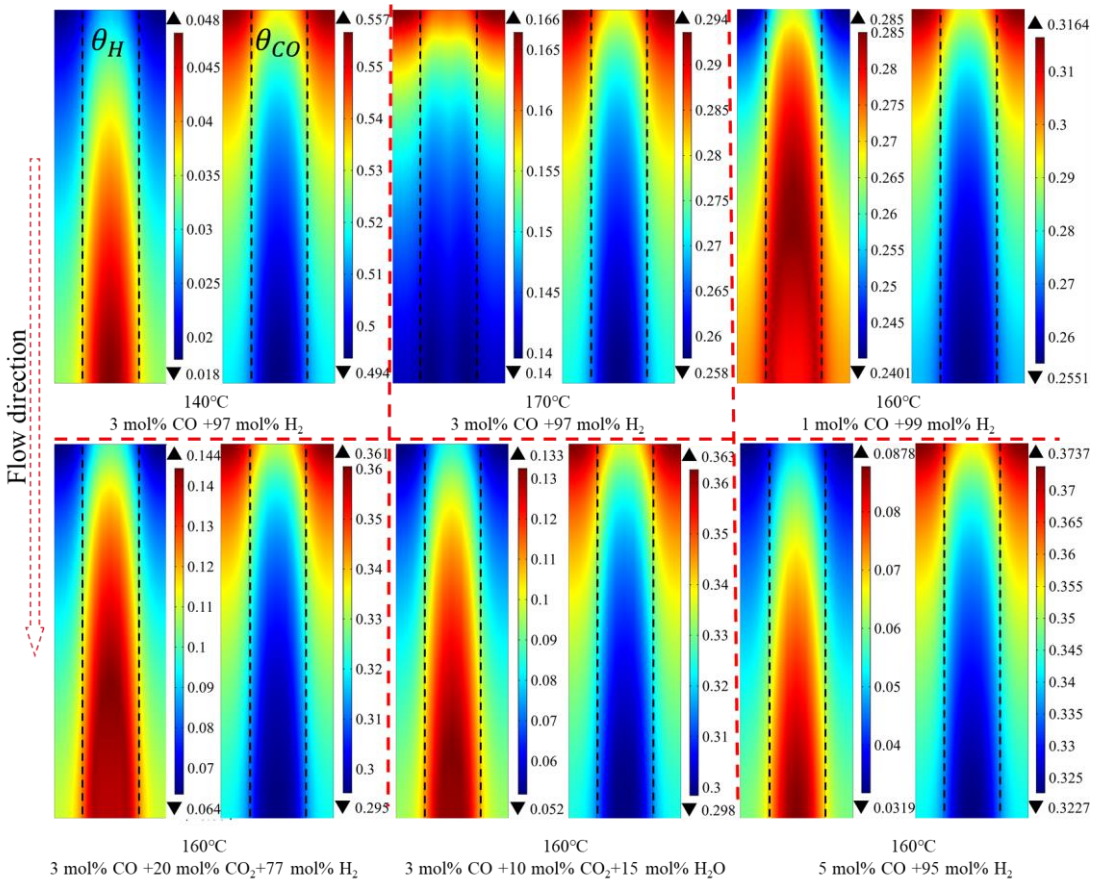

Fig. 12. Distribution of the H_2 coverage and the CO coverage over the middle of ACL of the middle-cell at an average voltage of 0.3V under different operation conditions. Left: H_2 coverage, Right: CO coverage.

4. Conclusion

To understand the details about the effects of CO poisoning on the HT-PEMFC stack, especially on the multi-cell stack, a numerical model has been established and numerical simulation of three different stacks with different numbers of cells has been conducted. The novelties of the manuscript can be concluded as follows: 1)The kinetics parameters

of CO poisoning are corrected by comparing the simulation results with the experimental results; 2)The performance, H_2 coverage, CO coverage and temperature of different stacks and different individual cells in a stack are compared at 160°C with 3 mol% CO in H_2, as well as the effects of operating temperature, CO concentration, CO_2 concentration and vapor concentration are investigated. It is found that the stack with more cells shows better performance, higher volume average H_2 coverage and lower volume average CO coverage because of the higher temperature inside. The average power density at 0.3V of the five-cell stack is 8.9%, 2.8% higher than that of single-cell stack and three-cell stack, respectively. In addition, the tolerance to CO varied between cells in a stack due to the temperature distribution difference, and the closer the cell is in the middle, the better the tolerance is. Since the temperature on the cathode side (Y>0) is higher, which makes the cell closer to the cathode side of the stack performs better than the one closer to the anode side. It also can be found that increasing operation temperature can increase the resistance to CO poisoning and can increase performance. However, too high temperature not only reduce the CO coverage but also reduce the H_2 coverage, increasing anode overpotential. When the average voltage is 0.3V and the CO content in H_2 is 3 mol%, increasing the operating temperature from 140°C to 170°C increases the performance by 1.06 times, the H_2 coverage increases by 1.38 times, and the CO coverage decreases by 0.47 times. With the increase of CO_2 and water vapor in anode gas, the H_2 coverage decreases and the CO coverage increases due to the decrease of H_2 concentration. When the concentration of CO_2 increases from 5 mol% to 20 mol%, the power density and H_2 coverage decrease 5.4%, 29.7%, respectively, and CO coverage increases 0.08%. When the concentration of H_2O increases from 1 mol% to 15 mol%, the power density and H_2 coverage decrease 6.98%, 34.8%, respectively, and CO coverage increases 1.68%.

Nomenclature

A	area, m^2	$\overline{\rho_{Pt}}$	molar area density of catalyst sites,mol/m^2
a	the ratio of reaction surface to CL volume	μ	dynamic viscosity, $kg/(m \cdot s)$
		x	mole fraction, mol%
ACL	anode catalyst layer	η	overpotential, V
BP	bipolar plate	χ	coefficient of thermal expansion, $1/K$
C	molar concentration, mol/m^3	λ	the number of affected sites per CO site for hydrogen adsorption
CC	coolant channel	φ	phase potential, V
CL	catalyst layer	φ	phase potential, V

CCL	cathode catalyst layer	α	Transfer coefficient
CO	carbon monoxide	q	heat flux, W/m^2
C_p	specific heat capacity, $\mathrm{J/(kg \cdot K)}$	$\delta(\Delta E_H)$	variation of activation energy for H_2 dissociative adsorption near CO occupied the site
DL	the doping level of phosphoric acid in membrane	$\delta(\Delta G_{CO})$	the difference of free energy of CO adsorption between $\theta_{CO} = 1$ and $\theta_{CO} = 0$
D	diffusion coefficients, m^2/s	θ	coverage on Pt
E_{eq}	Equilibrium potential, V	k_{eh}	electro-oxidation rate of H_2
GDL	gas diffusion layer	b_{dh}	desorption ratio of H_2
GC	gas flow channel	k_{ah}	adsorption rate of H_2
K	permeability, $\mathrm{m^2}$	b_{dc}	desorption ratio of CO
R	universal gas constant, $8.3145 J/(K \cdot mol)$	k_{ac}	adsorption rate of CO
T_{opt}	Operation temperature, K	k_{ec}	electro-oxidation rate of CO
M	molecular weight, g/mol	**Subscripts and Superscripts**	
MEM	membrane	g	gas
S	source term in the conservation equation	m	mass equation
I	current density, A/cm^2	u	momentum equation
F	Faraday constant, $96487\ \mathrm{C/mol}$	i, j	species index
κ	Electrical/proton conductivity, $\mathrm{S/m}$	ele	electronic
		ion	ionic
k	thermal conductivity, $\mathrm{W/(m \cdot K)}$	in	the inlet of gas channel
p	pressure, Pa	H	Hydrogen atom
ζ	stoichiometric ratio	a, c	anode, cathode
γ	the volume fraction of electrolyte in CL	H_2, O_2	hydrogen, oxygen
∇	Hamiltonian operator	eff	effective value in the porous region
ρ	density, $\mathrm{kg/m^3}$	ref	reference
$\vec{u}$	velocity, $\mathrm{m/s}$		
ω	mass fraction		

Acknowledgment

This work is supported in part by the national natural science foundation of China (51806024), the Technological Innovation and Application Demonstration in Chongqing (Major Themes of Industry: cstc2019jscx-fxyd0158, cstc2019jscx-zdztzxX0033). M. Ni thanks the grants (Project Number: PolyU 152214/17E and PolyU 152064/18E) from Research Grant Council, University Grants Committee, Hong Kong SAR.

Reference

[1] X. Xu, W. Yang, X. Zhuang, B. Xu, Experimental and numerical investigation on effects of cathode flow field configurations in an air-breathing high-temperature PEMFC, Int. J. Hydrogen Energy 44(45) (2019) 25010-25020.

[2] Z. Yang, K. Jiao, Z. Liu, Y. Yin, Q. Du, Investigation of performance heterogeneity of PEMFC stack based on 1+1D and flow distribution models, Energy Convers. Manage. 207 (2020).

[3] B. Zhang, F. Lin, C. Zhang, R. Liao, Y.-X. Wang, Design and implementation of model predictive control for an open-cathode fuel cell thermal management system, Renewable Energy 154 (2020) 1014-1024.

[4] S.A. Grigoriev, V.N. Fateev, D.G. Bessarabov, P. Millet, Current status, research trends, and challenges in water electrolysis science and technology, Int. J. Hydrogen Energy 45(49) (2020) 26036-26058.

[5] F. Zhou, S.J. Andreasen, S.K. Kær, J.O. Park, Experimental investigation of carbon monoxide poisoning effect on a PBI/H3PO4 high temperature polymer electrolyte membrane fuel cell: Influence of anode humidification and carbon dioxide, Int. J. Hydrogen Energy 40(43) (2015) 14932-14941.

[6] D.G. Lopes, E.P. da Silva, C.S. Pinto, N.P. Neves, J.C. Camargo, P.F.P. Ferreira, A.L. Furlan, D.G. Lopes, Technical and economic analysis of a power supply system based on ethanol reforming and PEMFC, Renewable Energy 45 (2012) 205-212.

[7] M. Al-Zareer, I. Dincer, M.A. Rosen, Production of hydrogen-rich syngas from novel processes for gasification of petroleum cokes and coals, Int. J. Hydrogen Energy 45(20) (2020) 11577-11592.

[8] I.V. Pushkareva, A.S. Pushkarev, S.A. Grigoriev, P. Modisha, D.G. Bessarabov, Comparative study of anion exchange membranes for low-cost water electrolysis, Int. J. Hydrogen Energy 45(49) (2020) 26070-26079.

[9] M. Li, Y. Bai, C. Zhang, Y. Song, S. Jiang, D. Grouset, M. Zhang, Review on the research of hydrogen storage system fast refueling in fuel cell vehicle, Int. J. Hydrogen Energy 44(21) (2019) 10677-10693.

[10] L. Barelli, G. Bidini, F. Gallorini, S. Servili, Hydrogen production through sorption-enhanced steam methane reforming and membrane technology: A review, Energy 33(4) (2008) 554-570.

[11] A. Chandan, M. Hattenberger, A. El-kharouf, S. Du, A. Dhir, V. Self, B.G. Pollet, A. Ingram, W. Bujalski, High temperature (HT) polymer electrolyte membrane fuel cells (PEMFC) – A review, J. Power Sources 231 (2013) 264-278.

[12] P. Ribeirinha, I. Alves, F.V. Vázquez, G. Schuller, M. Boaventura, A. Mendes, Heat integration of methanol steam reformer with a high-temperature polymeric electrolyte membrane fuel cell, Energy 120 (2017) 468-477.

[13] F. Salimi Nanadegani, E. Nemati Lay, B. Sunden, Computational analysis of the impact of a micro porous layer (MPL) on the characteristics of a high temperature PEMFC, Electrochim. Acta 333 (2020).

[14] X. Guo, H. Zhang, Performance analyses of a combined system consisting of high-temperature polymer electrolyte membrane fuel cells and thermally regenerative electrochemical cycles, Energy 193 (2020).

[15] M. Bornapour, R.-A. Hooshmand, M. Parastegari, An efficient scenario-based stochastic programming method for optimal scheduling of CHP-PEMFC, WT, PV and hydrogen storage units in micro grids, Renewable Energy 130 (2019) 1049-1066.

[16] R. Haider, Y. Wen, Z.F. Ma, D.P. Wilkinson, L. Zhang, X. Yuan, S. Song, J. Zhang, High temperature proton exchange membrane fuel cells: progress in advanced materials and key technologies, Chem. Soc. Rev. (2020).

[17] S.S. Araya, F. Zhou, V. Liso, S.L. Sahlin, J.R. Vang, S. Thomas, X. Gao, C. Jeppesen, S.K. Kær, A comprehensive review of PBI-based high temperature PEM fuel cells, Int. J. Hydrogen Energy 41(46) (2016) 21310-21344.

[18] M. Yu, H. Sun, T. Zhang, Q. Li, J. Li, X. Zhang, Current density distribution in an HT-PEM fuel cell with a poly (2, 5-benzimidazole) membrane, Int. J. Hydrogen Energy (2020).

[19] W.-M. ACS Symposium SeriesYan, G.-Y. Cheng, C.-Y. Chen, T.-F. Yang, M. Ghalambaz, Effects

650 of reformate on performance of PBI/H3PO4 proton exchange membrane fuel cell stack, Int. J. Hydrogen
651 Energy 45(30) (2020) 15346-15357.
652 [20] C. Zhang, T. Yu, J. Yi, Z. Liu, K.A.R. Raj, L. Xia, Z. Tu, S.H. Chan, Investigation of heating and
653 cooling in a stand-alone high temperature PEM fuel cell system, Energy Convers. Manage. 129 (2016) 36-
654 42.
655 [21] R.K. Abdul Rasheed, C. Zhang, S.H. Chan, Numerical analysis of high-temperature proton
656 exchange membrane fuel cells during start-up by inlet gas heating and applied voltage, Int. J. Hydrogen
657 Energy 42(15) (2017) 10390-10406.
658 [22] R.K. Abdul Rasheed, S.M.M. Ehteshami, S.H. Chan, Analytical modelling of boiling phase
659 change phenomenon in high-temperature proton exchange membrane fuel cells during warm-up process,
660 Int. J. Hydrogen Energy 39(5) (2014) 2246-2260.
661 [23] G. Varghese, V. Babu K.P, T.V. Joseph, P. Chippar, A Numerical Investigation on Thermal
662 Gradients and Stresses in High Temperature PEM Fuel Cell During Start-up, Int. J. Heat Mass Transfer 175
663 (2021).
664 [24] L. Xia, C. Zhang, M. Hu, S. Jiang, C.S. Chin, Z. Gao, Q. Liao, Investigation of parameter effects
665 on the performance of high-temperature PEM fuel cell, Int. J. Hydrogen Energy 43(52) (2018) 23441-23449.
666 [25] C.-Y. Chen, S.-C. Su, Development and performance evaluation of a high temperature proton
667 exchange membrane fuel cell with stamped 304 stainless steel bipolar plates, Int. J. Hydrogen Energy 43(29)
668 (2018) 13430-13439.
669 [26] K. Sasiwimonrit, W.-C. Chang, To improve the high temperature polymer electrolyte membrane
670 fuel cells performance by altering the properties of catalyst layer, Int. J. Hydrogen Energy 45(28) (2020)
671 14491-14499.
672 [27] K. Jiao, X. Li, A Three-Dimensional Non-isothermal Model of High Temperature Proton
673 Exchange Membrane Fuel Cells with Phosphoric Acid Doped Polybenzimidazole Membranes, Fuel Cells
674 10(3) (2010) 351-362.
675 [28] P. Ribeirinha, M. Abdollahzadeh, J.M. Sousa, M. Boaventura, A. Mendes, Modelling of a high-
676 temperature polymer electrolyte membrane fuel cell integrated with a methanol steam reformer cell,
677 Applied Energy 202 (2017) 6-19.
678 [29] Y. Yang, H. Zhang, P. Yan, K. Jermsittiparsert, Multi-objective optimization for efficient modeling
679 and improvement of the high temperature PEM fuel cell based Micro-CHP system, Int. J. Hydrogen Energy
680 45(11) (2020) 6970-6981.
681 [30] A. Arsalis, M.P. Nielsen, S.K. Kær, Modeling and optimization of a 1 kWe HT-PEMFC-based
682 micro-CHP residential system, Int. J. Hydrogen Energy 37(3) (2012) 2470-2481.
683 [31] F. Zhou, D. Singdeo, S.K. Kær, Investigation of the Effect of Humidity Level of H_2 on Cell
684 Performance of a HT-PEM Fuel Cell, Fuel Cells 19(1) (2019) 2-9.
685 [32] Q. Li, R. He, J.-A. Gao, J.O. Jensen, N.J. Bjerrum, The CO Poisoning Effect in PEMFCs
686 Operational at Temperatures up to 200°C, J. Electrochem. Soc. 150(12) (2003).
687 [33] S.K. Das, A. Reis, K.J. Berry, Experimental evaluation of CO poisoning on the performance of a
688 high temperature proton exchange membrane fuel cell, J. Power Sources 193(2) (2009) 691-698.
689 [34] Y. Devrim, A. Albostan, H. Devrim, Experimental investigation of CO tolerance in high
690 temperature PEM fuel cells, Int. J. Hydrogen Energy 43(40) (2018) 18672-18681.
691 [35] A. Bergmann, D. Gerteisen, T. Kurz, Modelling of CO Poisoning and its Dynamics in HTPEM
692 Fuel Cells, Fuel Cells 10(2) (2010) 278-287.
693 [36] F.J. Pinar, M. Rastedt, N. Pilinski, P. Wagner, A. Dyck, Demonstrating feasibility of a high

694 temperature polymer electrolyte membrane fuel cell operation with natural gas reformate composition, Int.
695 J. Hydrogen Energy 42(19) (2017) 13860-13875.
696 [37] C. Zhang, W. Zhou, M.M. Ehteshami, Y. Wang, S.H. Chan, Determination of the optimal
697 operating temperature range for high temperature PEM fuel cell considering its performance, CO tolerance
698 and degradation, Energy Convers. Manage. 105 (2015) 433-441.
699 [38] A. Moradi Bilondi, M. Abdollahzadeh, M.J. Kermani, H. Heidary, P. Havaej, Numerical study of
700 anode side CO contamination effects on PEM fuel cell performance; and mitigation methods, Energy
701 Convers. Manage. 177 (2018) 519-534.
702 [39] M. Abdollahzadeh, P. Ribeirinha, M. Boaventura, A. Mendes, Three-dimensional modeling of
703 PEMFC with contaminated anode fuel, Energy 152 (2018) 939-959.
704 [40] S.M.M. Ehteshami, S.H. Chan, Computational fluid dynamics simulation of polymer electrolyte
705 membrane fuel cells operating on reformate, Electrochim. Acta 56(5) (2011) 2276-2283.
706 [41] W.-M. Yan, H.-S. Chu, M.-X. Lu, F.-B. Weng, G.-B. Jung, C.-Y. Lee, Degradation of proton
707 exchange membrane fuel cells due to CO and CO2 poisoning, J. Power Sources 188(1) (2009) 141-147.
708 [42] K. Jiao, I.E. Alaefour, X. Li, Three-dimensional non-isothermal modeling of carbon monoxide
709 poisoning in high temperature proton exchange membrane fuel cells with phosphoric acid doped
710 polybenzimidazole membranes, Fuel 90(2) (2011) 568-582.
711 [43] K. Jiao, Y. Zhou, Q. Du, Y. Yin, S. Yu, X. Li, Numerical simulations of carbon monoxide
712 poisoning in high temperature proton exchange membrane fuel cells with various flow channel designs,
713 Applied Energy 104 (2013) 21-41.
714 [44] J.J. Baschuk, X. Li, Modelling CO poisoning and O2 bleeding in a PEM fuel cell anode,
715 International Journal of Energy Research 27(12) (2003) 1095-1116.
716 [45] R.K. Abdul Rasheed, S.H. Chan, Transient carbon monoxide poisoning kinetics during warm-up
717 period of a high-temperature PEMFC – Physical model and parametric study, Applied Energy 140 (2015)
718 44-51.
719 [46] K.A.R. Raj, S.H. Chan, Transient analysis of carbon monoxide transport phenomena and
720 adsorption kinetics in HT-PEMFC during dynamic current extraction, Electrochim. Acta 165 (2015) 288-
721 300.
722 [47] R. Kamal, S.H. Chan, Sensitivity analysis of anode overpotential during start-up process of a high
723 temperature proton exchange membrane fuel cell, Electrochim. Acta 176 (2015) 965-975.
724 [48] K. Oh, G. Jeong, E. Cho, W. Kim, H. Ju, A CO poisoning model for high-temperature proton
725 exchange membrane fuel cells comprising phosphoric acid-doped polybenzimidazole membranes, Int. J.
726 Hydrogen Energy 39(36) (2014) 21915-21926.
727 [49] K. Oh, H. Ju, Temperature dependence of CO poisoning in high-temperature proton exchange
728 membrane fuel cells with phosphoric acid-doped polybenzimidazole membranes, Int. J. Hydrogen Energy
729 40(24) (2015) 7743-7753.
730 [50] T.E. Springer, T. Rockward, T.A. Zawodzinski, S. Gottesfeld, Model for Polymer Electrolyte Fuel
731 Cell Operation on Reformate Feed: Effects of CO, H 2 Dilution, and High Fuel Utilization, J. Electrochem.
732 Soc. 148(1) (2001) A11-A23.
733 [51] L. Lüke, H. Janßen, M. Kvesić, W. Lehnert, D. Stolten, Performance analysis of HT-PEFC stacks,
734 Int. J. Hydrogen Energy 37(11) (2012) 9171-9181.
735 [52] T. Sousa, M. Mamlouk, K. Scott, An isothermal model of a laboratory intermediate temperature
736 fuel cell using PBI doped phosphoric acid membranes, Chem. Eng. Sci. 65(8) (2010) 2513-2530.
737 [53] J. Zhang, C. Zhang, D. Hao, M. Ni, S. Huang, D. Liu, Y. Zheng, 3D non-isothermal dynamic
738 simulation of high temperature proton exchange membrane fuel cell in the start-up process, Int. J. Hydrogen

739 Energy 46(2) (2021) 2577-2593.
740 [54] D. Singdeo, T. Dey, P.C. Ghosh, Modelling of start-up time for high temperature polymer
741 electrolyte fuel cells, Energy 36(10) (2011) 6081-6089.
742 [55] P. Ren, P. Pei, Y. Li, Z. Wu, D. Chen, S. Huang, Degradation mechanisms of proton exchange
743 membrane fuel cell under typical automotive operating conditions, Prog. Energy Combust. Sci. 80 (2020).
744 [56] S.-J. Cheng, J.-M. Miao, S.-J. Wu, Investigating the effects of operational factors on PEMFC
745 performance based on CFD simulations using a three-level full-factorial design, Renewable Energy 39(1)
746 (2012) 250-260.
747 [57] S. Li, B. Sundén, Three-dimensional modeling and investigation of high temperature proton
748 exchange membrane fuel cells with metal foams as flow distributor, Int. J. Hydrogen Energy 42(44) (2017)
749 27323-27333.
750 [58] B.E. Poling, J.M. Prausnitz, J.P. O'Connell, The Properties of Gases and Liquids, 5th Edition
751 123(27) (2001) 467-803.
752 [59] Inamuddin, T.A. Cheema, S.M.J. Zaidi, S.U. Rahman, Three dimensional numerical
753 investigations for the effects of gas diffusion layer on PEM fuel cell performance, Renewable Energy 36(2)
754 (2011) 529-535.
755 [60] Y. Luo, Q. Guo, Q. Du, Y. Yin, K. Jiao, Analysis of cold start processes in proton exchange
756 membrane fuel cell stacks, J. Power Sources 224 (2013) 99-114.
757
758
759

Mole fraction of CO (mol%)

Temperature (°C)

$\delta(\Delta G_{CO})$ (kJ/mol)

Mole fraction of CO (mol%)

Temperature (°C)

$\delta(\Delta E_H)$ (kJ/mol)

Second Current Distribution

Coverage of CO and H_2

Transport of Concentrated Species

Transport of Concentrated Species

Heat Transfer

Laminar Flow for Cooling

Free and Porous Media Flow

Free and Porous Media Flow

Cathode

Anode

Theory

Model validation

Stack simulation

Different stacks

Different cells in a stack

Results

Operation conditions

L=100mm

Pure O_2

H_2+CO

Symmetric boundary

Symmetric boundary

GC

GC

BP

GDL

CL

MEM

CL

GDL

BP

@125°C

@150°C

@175°C

@200°C

Voltage (V)

Current density (A/cm^2)

Temperature

H_2 coverage

CO coverage

Overpotential

Flow direction

Cell 1

Cell 2

Cell 3

Cell 4

Cell 5

Anode

Cathode

Reformate gas

Air

Coolant

MEM

BP

BP

GDL

CL

CL

GDL

GC

CC

L=100mm

Graphical Abstract

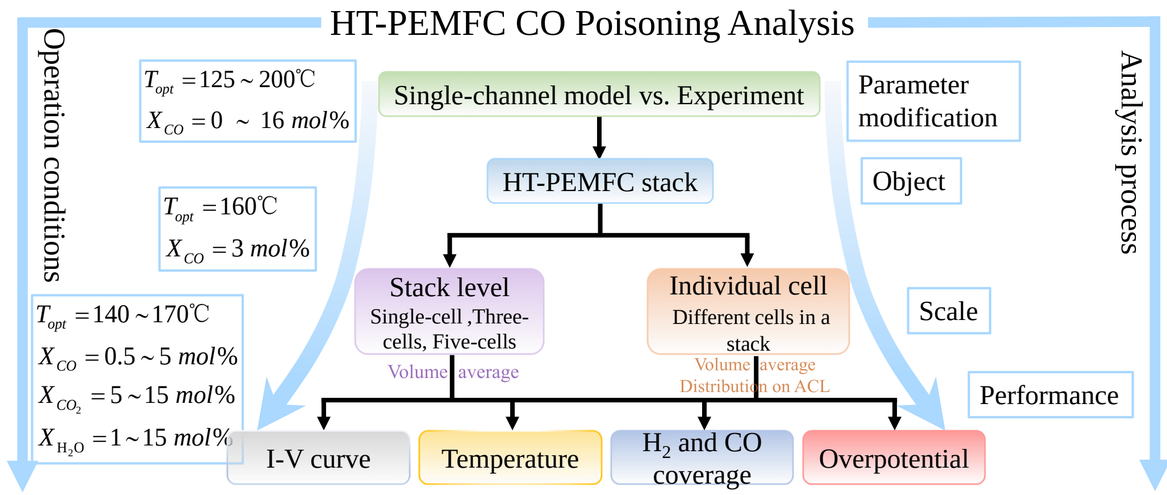

Fig.1. Schematic of multi-perspective analysis of HT-PEMFC CO poisoning

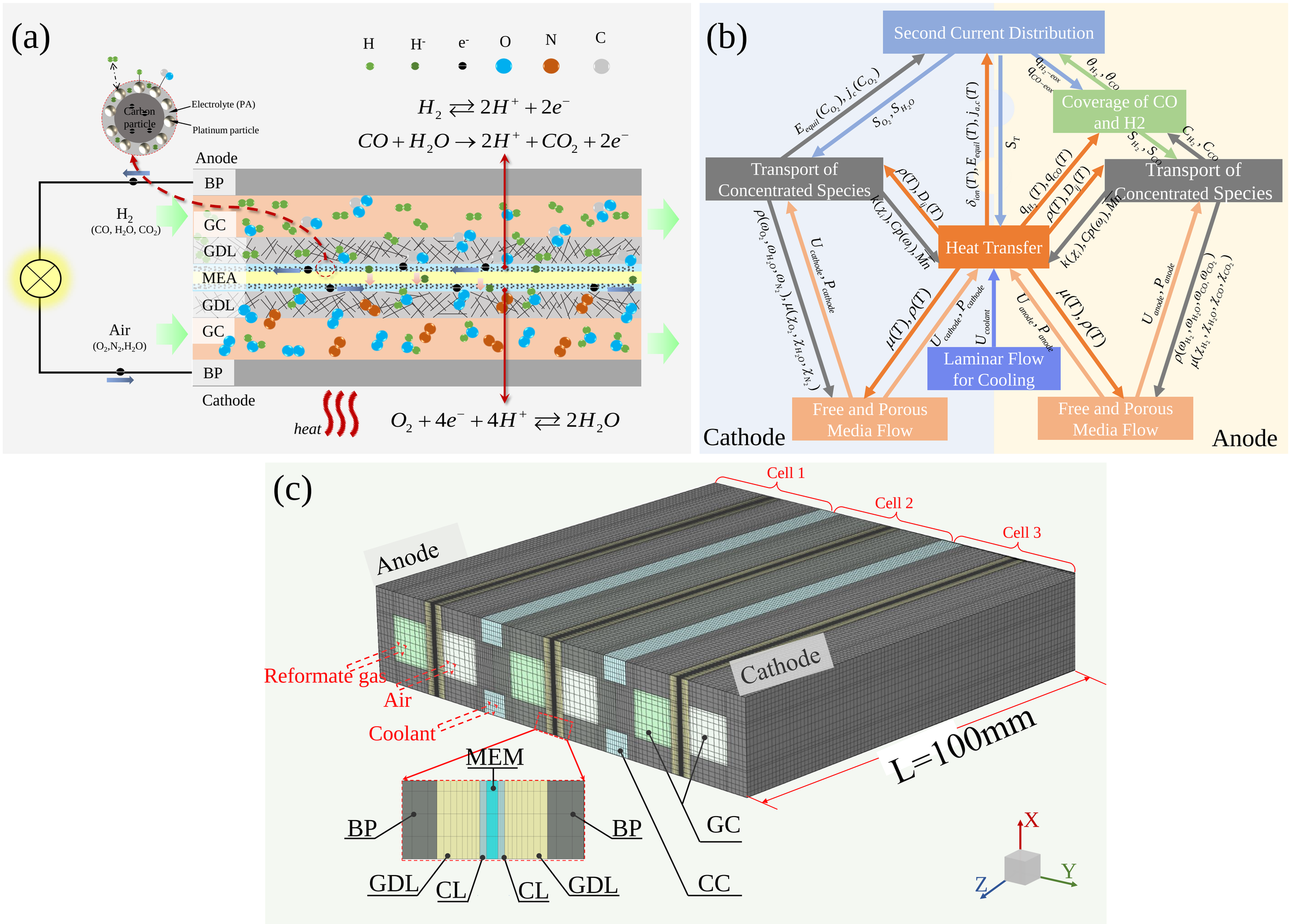

Fig. 2. (a) HT-PEMFC composition and working principle, (b) The coupling relationship between different physical fields, (c) Computational domain and mesh configuration of the three-cell stack.

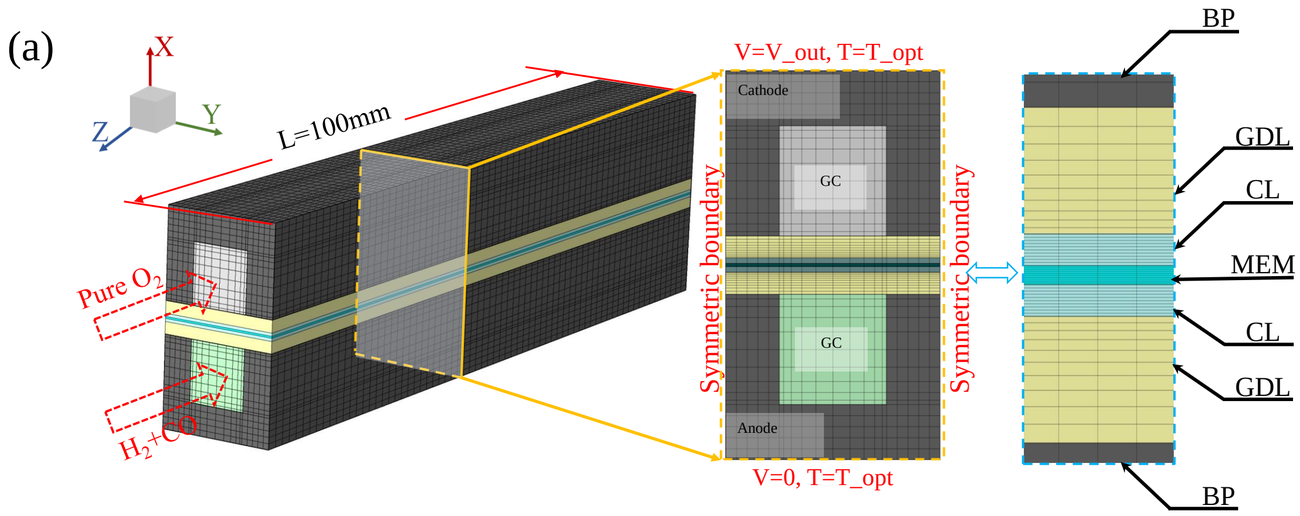

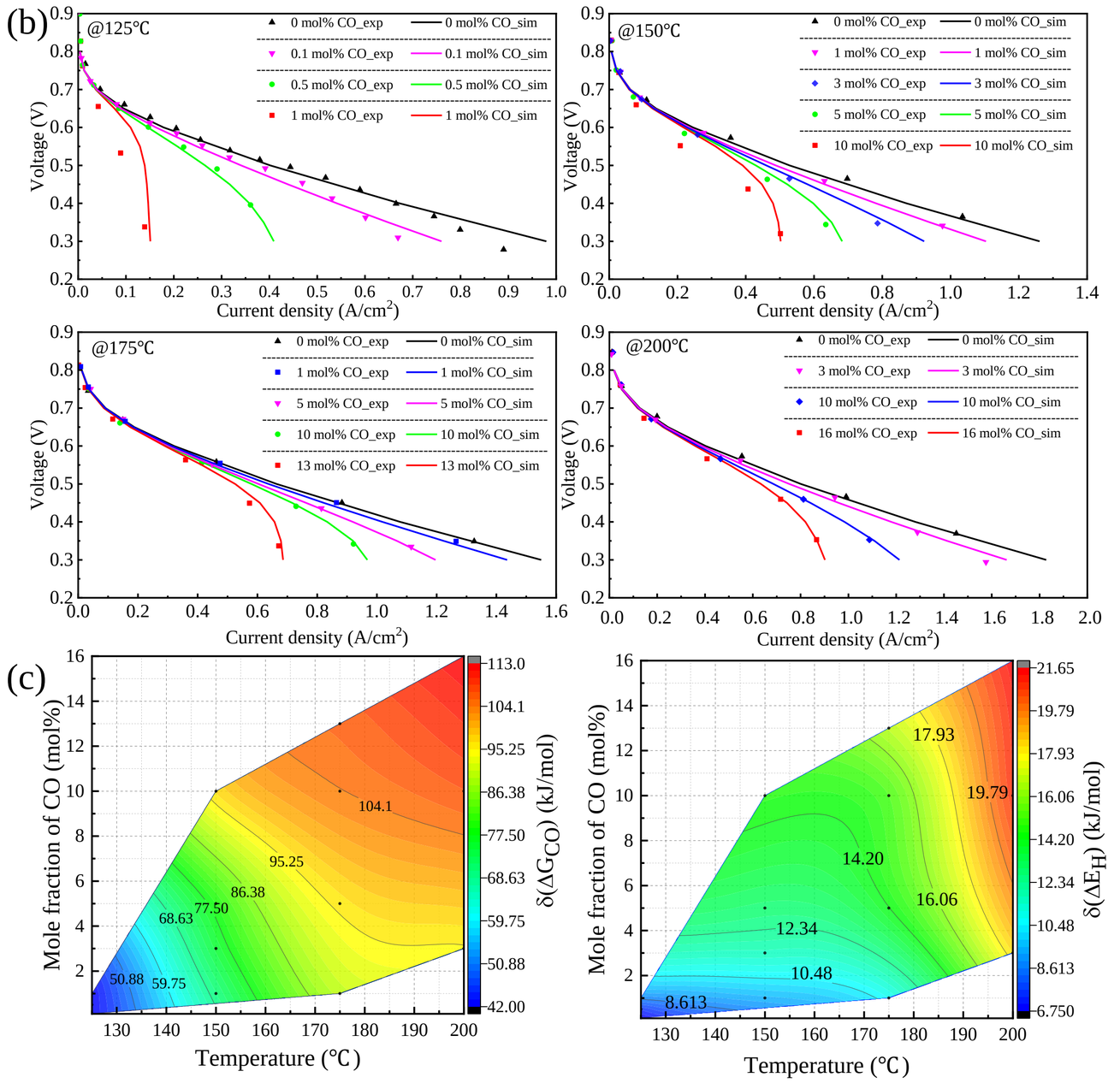

Fig. 3. Model validation. (a) Single-channel model for model validation, (b) The comparison between experimental results and simulation results at different temperatures and different CO mole fractions, (c) $\delta(\Delta G_{CO})$ and $\delta(\Delta E_H)$ change with temperature and CO mole fraction.

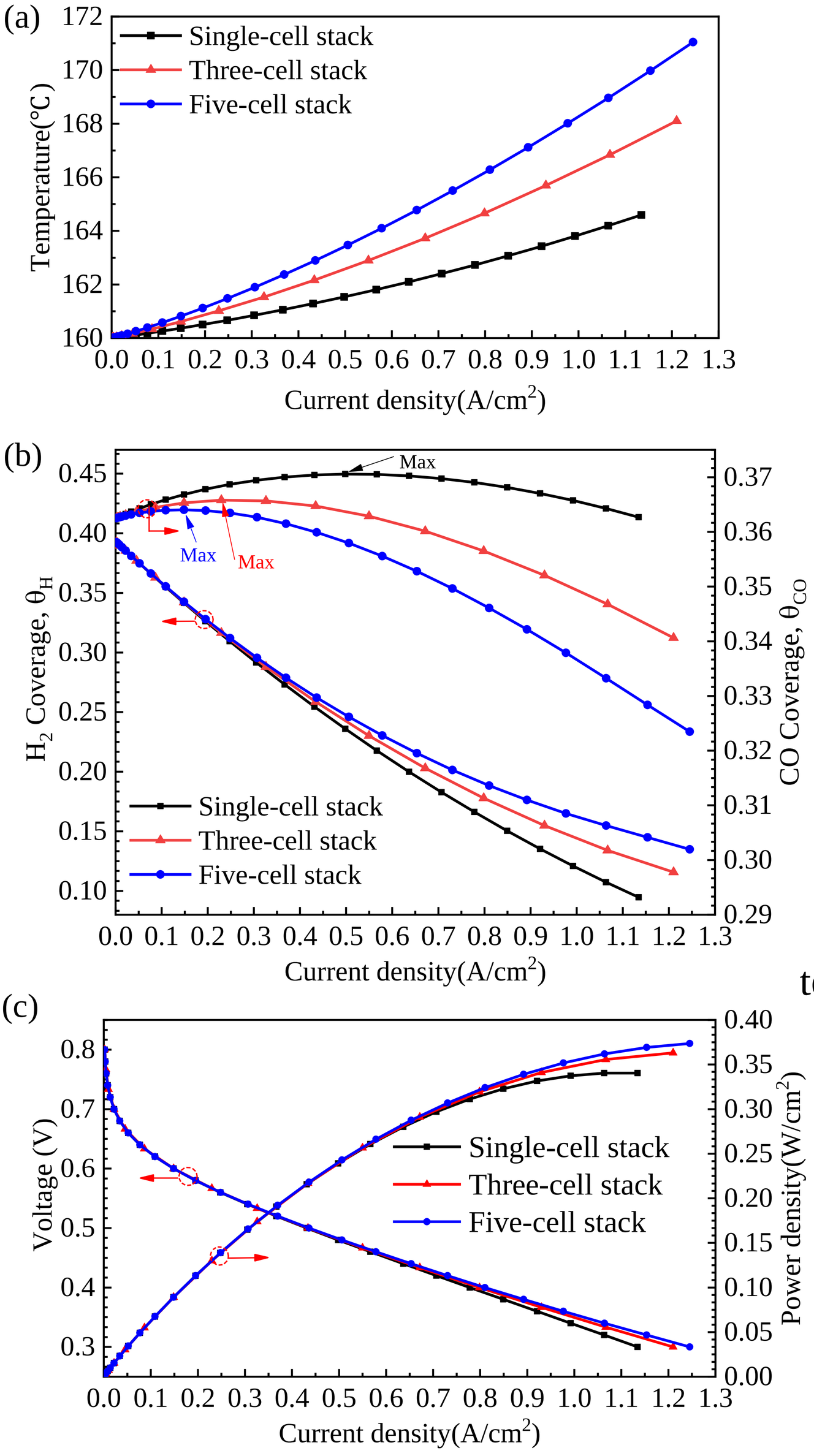

Fig. 4. Comparison of stacks with different numbers of cells at 160°C and 3 mol% CO contained in H_2. (a) Volume average temperature on MEA, (b) Volume average H_2 and CO coverage fractions on ACL, (c) Polarization curve.

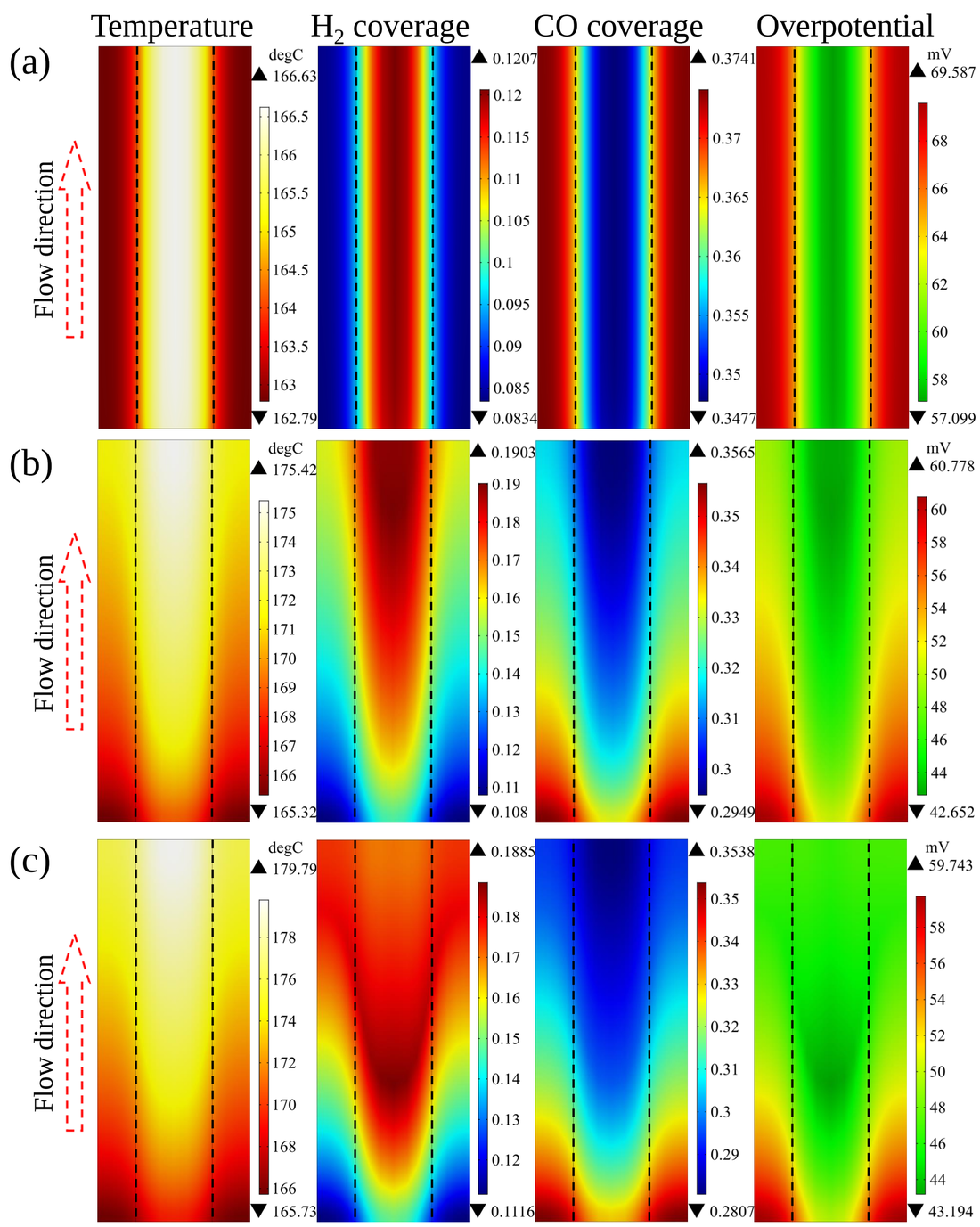

Fig. 5. Distribution of temperature, H_2 coverage, CO coverage and overpotential over the middle of the ACL of the middle-cell of different stacks at an average voltage of 0.3V. (a) Single-cell stack, (b) Three-cell stack, (c) Five-cell stack.

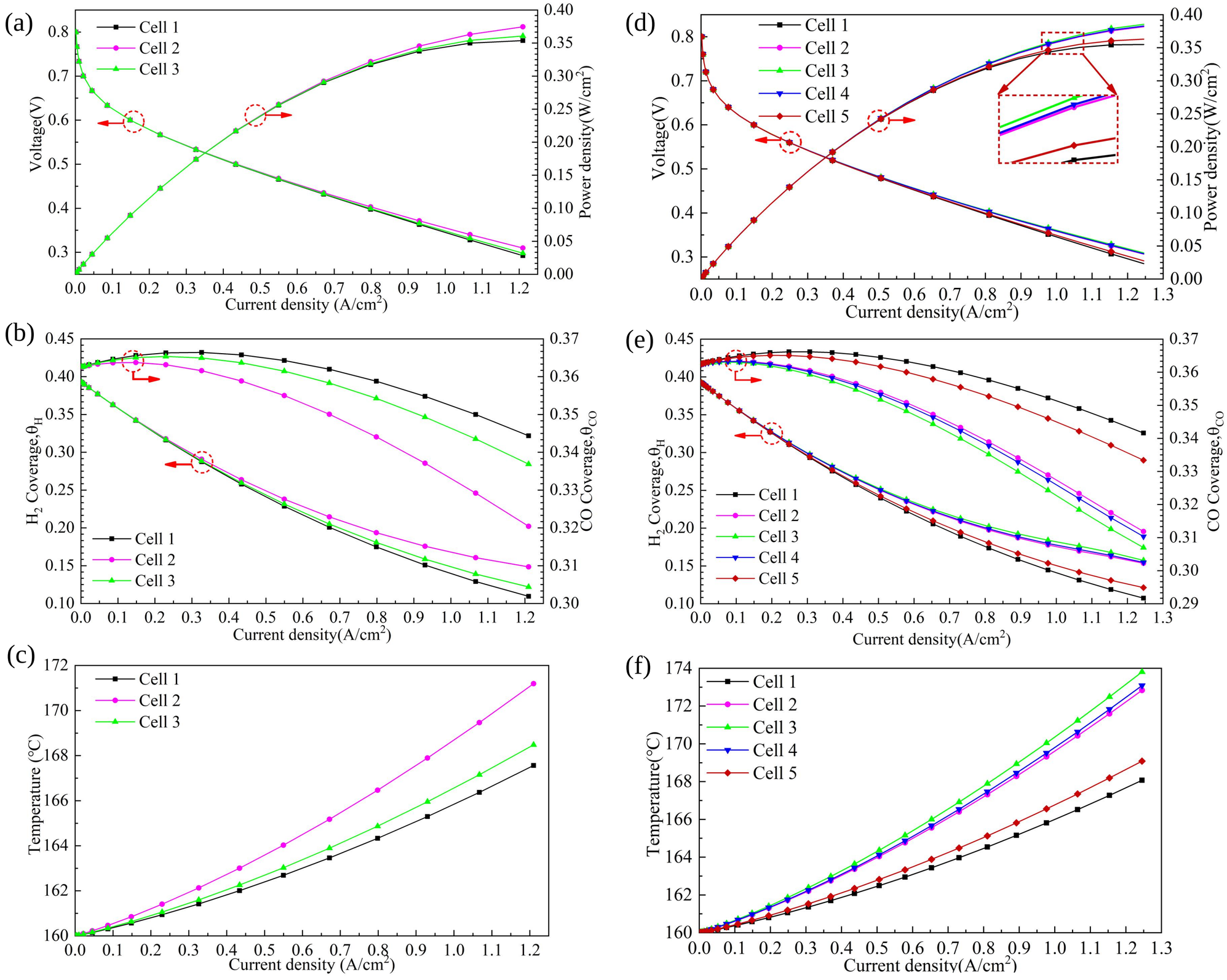

Fig. 6. Comparison between different cells in multi-cell stacks at 160oC and 3 mol% CO contained in H_2. (a)-(c) Three-cell stack, (d)-(f) Five-cell stack. (a) and (d) Polarization curve, (b) and (e) Volume average H_2 coverage and volume average CO coverage on ACL, (c) and (f) Volume average temperature on MEA.

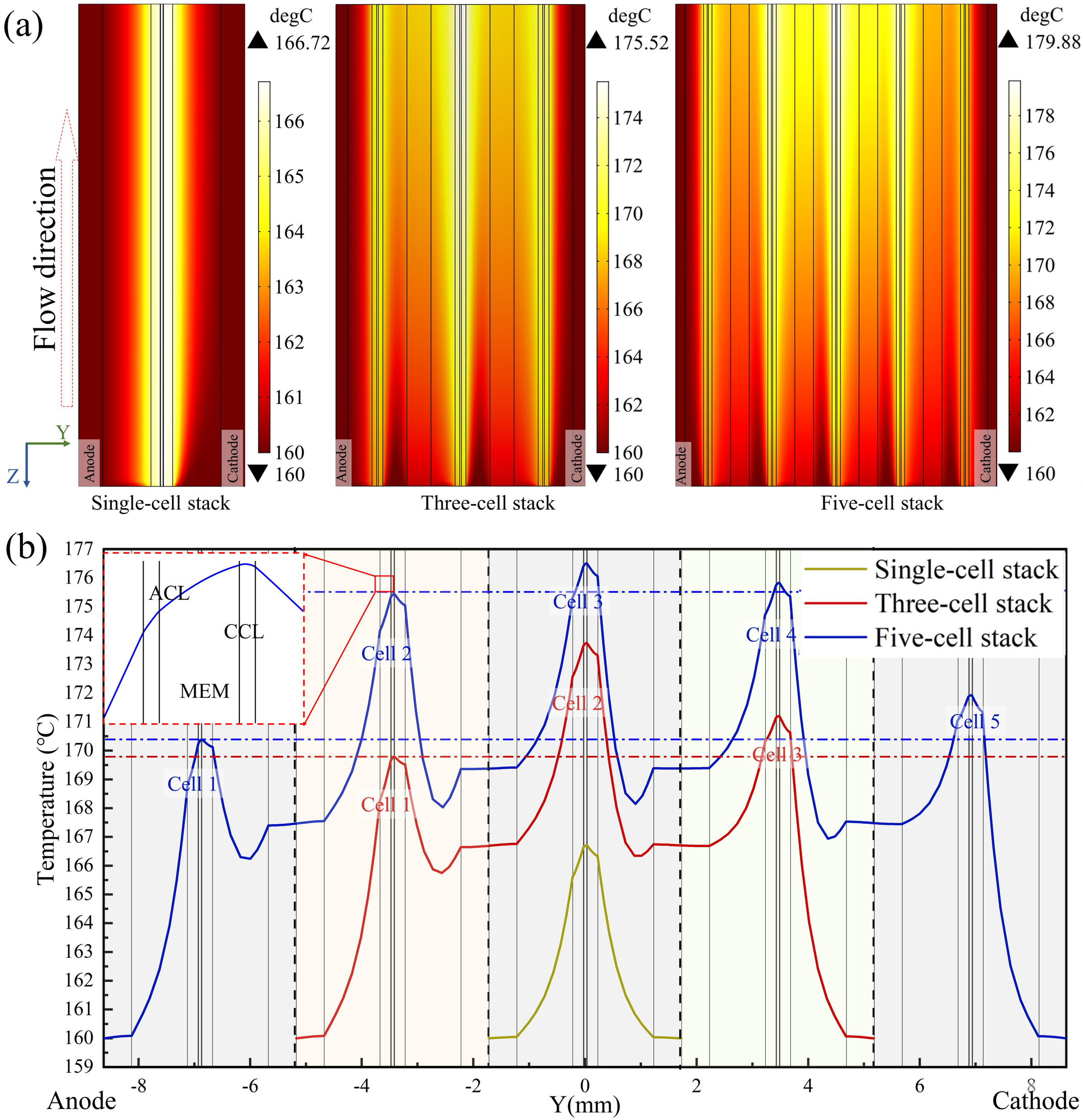

Fig. 7. Temperature distribution of stacks at an average voltage of 0.3V. (a) Along the gas channel at the middle plane (Z-Y plane), (b) Along the thickness direction of the stack (Z=50mm, Y direction).

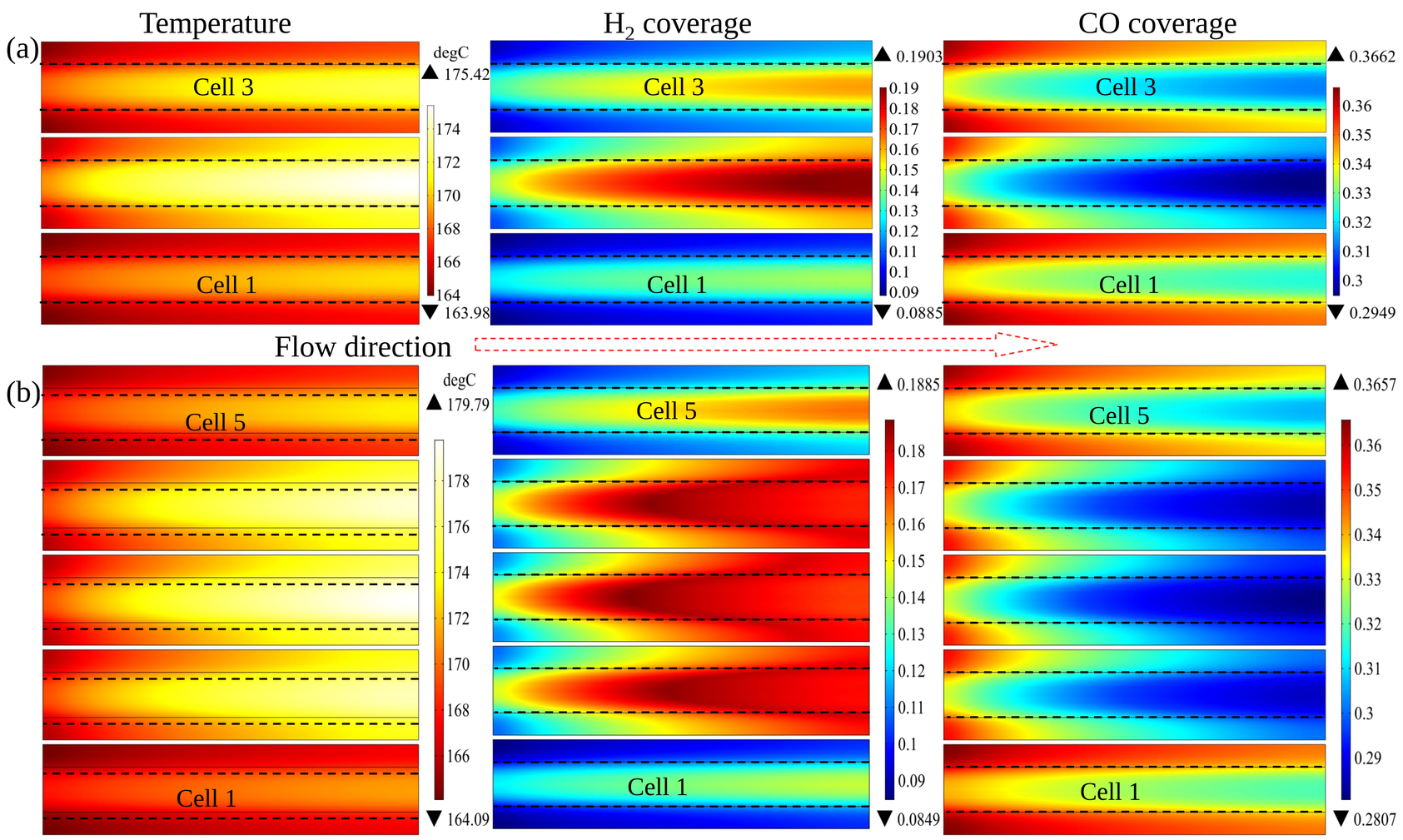

Fig.8. Comparison of temperature, H_2 coverage and CO coverage distribution over the middle of the ACL of different cells in the stack at an average voltage of 0.3V. (a) Three-cell stack, (b) Five-cell stack.

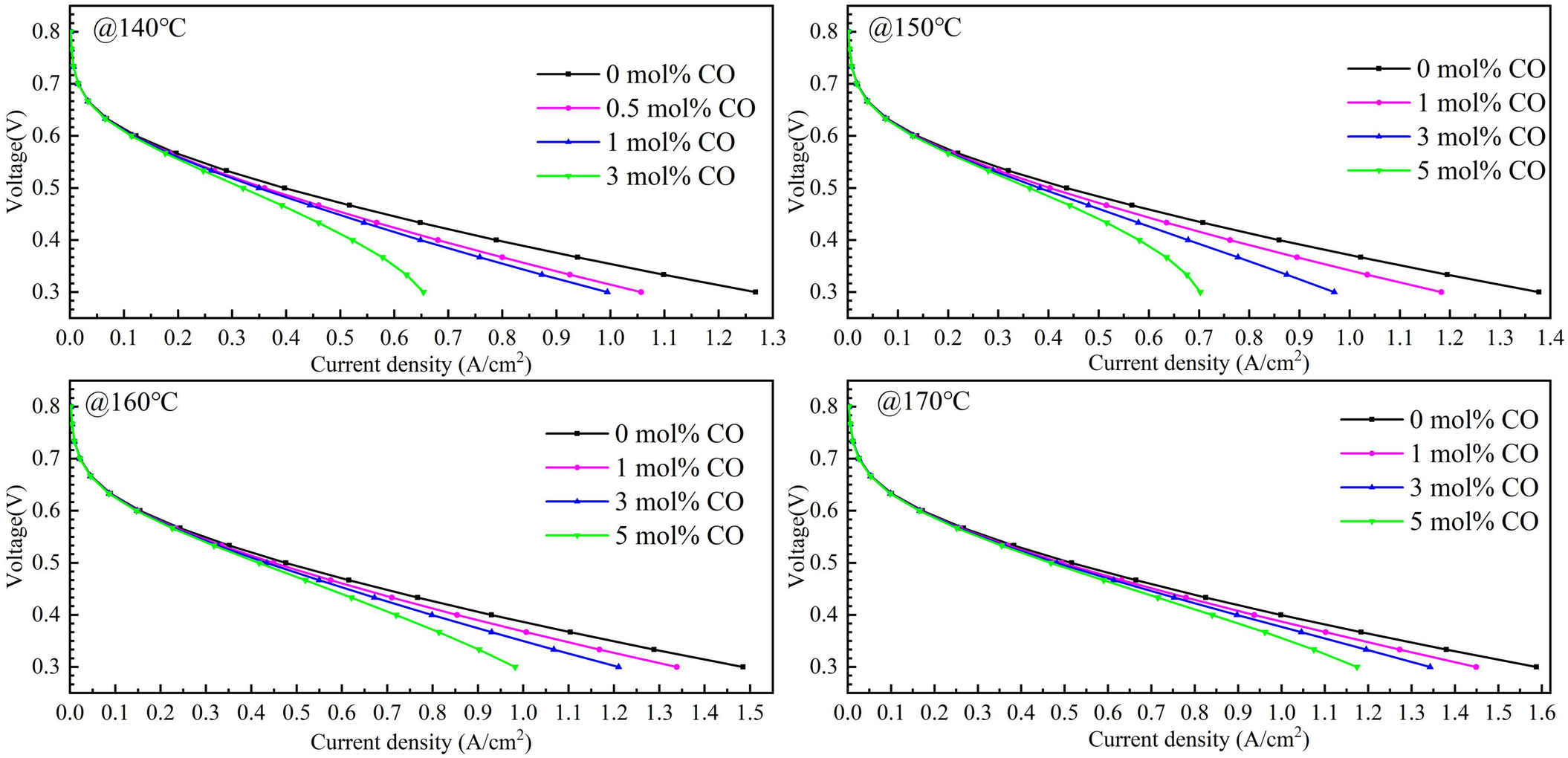

Fig. 9. Influence of operation temperature and mole fraction of CO on the performance of the three-cell stack.

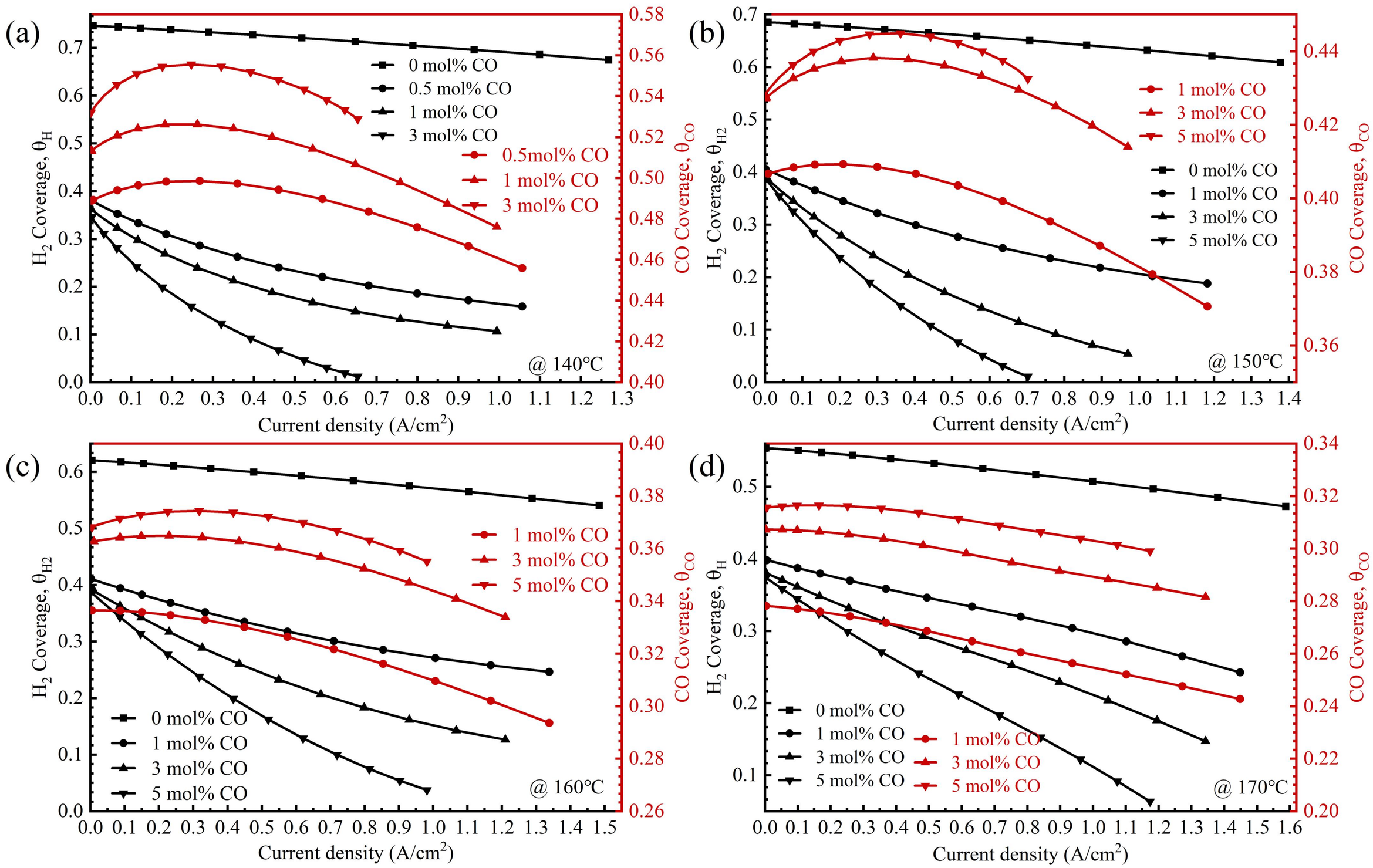

Fig. 10. Influence of operating temperature and mole fraction of CO on the volume average H_2 coverage and the volume average CO coverage at ACL of the three-cell stack.

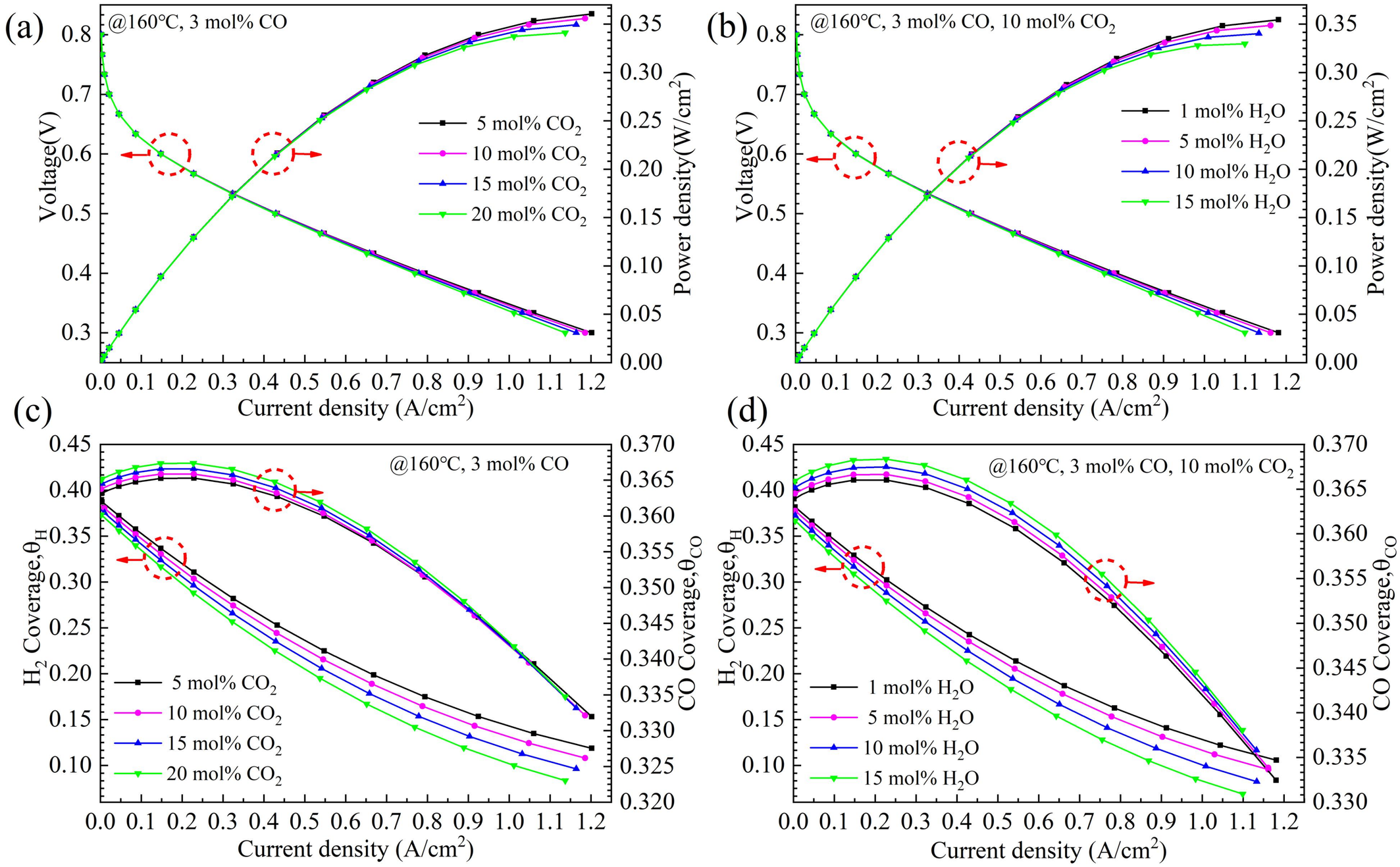

Fig. 11. Influence of mole fraction of CO_2 and H_2O on the three-cell stack. (a) and (b) The performance, (c) and (d) The volume average CO coverage and the volume average H_2 coverage.

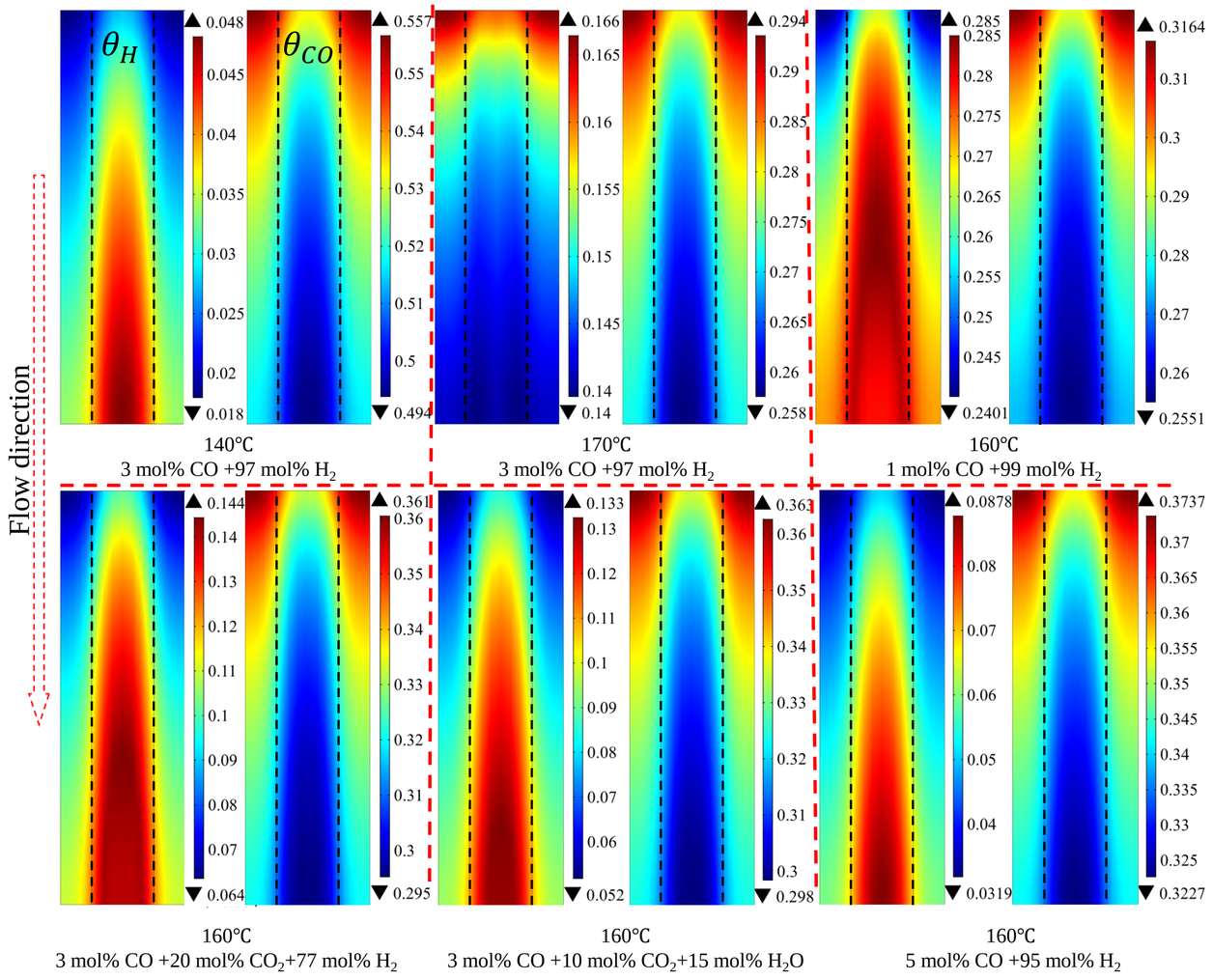

Fig.12. Distribution of the H_2 coverage and the CO coverage over the middle of ACL of the middle-cell at an average voltage of 0.3V under different operation conditions. Left: H_2 coverage, Right: CO coverage.